The Dissertation Committee for Wenting Fu Certifies that this is the approved version of the following dissertation:

Integrating In-Situ Measurements, Land Surface Models and Satellite Remote Sensing to Understand Impacts of Environmental Changes on Terrestrial Ecosystem Processes at Multiple Scales

Committee:

Robert E. Dickinson, Supervisor

Rong Fu

Zong-Liang Yang

Charles S. Jackson

Muhammad J. Shaikh

Integrating In-Situ Measurements, Land Surface Models and Satellite Remote Sensing to Understand Impacts of Environmental Changes on Terrestrial Ecosystem Processes at Multiple Scales

by

Wenting Fu, B.S.

Dissertation

Presented to the Faculty of the Graduate School of

The University of Texas at Austin

in Partial Fulfillment

of the Requirements

for the Degree of

Doctor of Philosophy

The University of Texas at Austin

May 2017

Acknowledgements

First of all, I would like to express my most sincere gratitude and appreciation to Dr. Robert E. Dickinson for his guidance, patience and encouragement throughout my years as a graduate student. This research would not have been possible without his support. I extend a thank you to Dr. Lianhong Gu, Dr. Jiafu Mao and Dr. Forrest Hoffman at Oak Ridge National Laboratory for the knowledge they shared with me that helped me to complete these studies. I would also like to thank the rest of my committee members, Dr. Rong Fu, Dr. Zong-Liang Yang, Dr. Charles Jackson, and Dr. Muhammad Shaikh for their insightful suggestions and comments that really help to refine this thesis. Additional gratitude is given to Dr. Ying Sun at Cornell University for her inspiration, and encouragement and offering me an example on becoming a great scientist. In addition, I would like to thank David Spindler for his tremendous help in resolving the technical issues in my studies.

I would like to thank each co-author of my dissertation manuscripts for everything that I learned from them, for their willingness to teach me and help me every time I asked them. I send a huge thank you to my friends and colleagues at the Jackson School of Geosciences for all the help and support they offered to me from day one.

Last but not least, I want to express my indebtedness to my dearest parents and my husband for giving me constant support and love during the completion of the thesis.

Integrating In-Situ Measurements, Land Surface Models and Satellite Remote Sensing to Understand Impacts of Environmental Changes on Terrestrial Ecosystem Processes at Multiple Scales

Wenting Fu, Ph.D.

The University of Texas at Austin, 2017

Supervisor: Robert E. Dickinson

How terrestrial ecosystems respond to environmental changes affects the well-being of human society. Thus, extreme climate events, increasing the atmospheric concentration of CO2, and drastic changes in temperature are sources of major concern. However, our current capacity to understand and predict these responses is still limited because a myriad of physical, chemical, and biological processes are involved. While many mechanistic-based land surface models have been developed, their performances remain relatively poor and require continuous improvement. While ground-based and space-based observational datasets of the surface of the Earth have been available for a long time, their linkages to the functional aspects of the processes in terrestrial ecosystems often are weak. In this study, I used the approach of integrating in-situ measurements, land surface models, and remote sensing by satellites. I hypothesized that, through such integration, the impacts of environmental changes on terrestrial processes at multiple scales could be better understood and even predicted, especially the impacts related to the functions of important ecosystems. I tested this hypothesis at the local, regional, and global scales.

At the local scale, i.e., at a Midwest forest site known as the isoprene volcano of the world, I examined the effects of droughts on the emissions of isoprene, which is the most abundant, non-methane, biogenic volatile organic compound. I compared flux tower observations with simulations performed by a state-of-the-art land model (CLM) coupled with the model of emissions of gases and aerosols from Nature version 2.1 (MEGAN2.1), and I used these observations to develop an understanding of how the amount of moisture in the soil and the ambient temperature affect the prediction of isoprene emissions during droughts. I found that temperature had a delaying effect on isoprene emissions, which are sensitive to variations in the moisture content of the soil. Thus, during drought conditions, both the delaying effect and the sensitivity to moisture are overlooked by the model. A better model that does not have these two shortcomings is required for realistic predictions of isoprene emissions.

At the regional scale, I investigated the potential of using sun-induced chlorophyll fluorescence (SIF) retrieved from a satellite to monitor vegetation activities in an arid region and a semi-arid region in Australia. I chose these two types of regions for this investigation because the ecosystems in such regions have important effects on the global carbon cycle, while their contributions are poorly constrained in global carbon budgets. I found that SIF was synchronized better with the activity of vegetation than other indices that are commonly used for this purpose. I quantified the relationships between the various activities of plants and the amount and frequency of precipitation, and I was able to demonstrate that, over the region being studied, SIF represented the activity of vegetation in response to the availability of water better than other, remotely-sensed variables.

At the global scale, I used multiple model ensembles to determine the climatic and anthropogenic controls on the terrestrial evapotranspiration trends from 1982 to

2010. After climatic influences, increases in CO2 were found to be the second-most dominant factor that affected the trend of ET. CO2 causes a decreasing trend in the canopy's transpiration and ET, and this is especially of concern for tropical forests and high-latitude shrub lands. The increased deposition of nitrogen amplifies the global ET slightly due to enhanced growth of plants. On a global scale, land-use-induced ET responses are minor, but they can be significant locally, particularly over regions with intensive changes in the land-cover. The results of my studies demonstrated that integrating in-situ measurements, models of the surface on the land, and remote sensing using satellites can provide insights regarding the impacts of environmental changes on terrestrial processes at multiple scales. This approach is particularly important when models are imperfect and observations are lacking. My findings indicated ways that future models can be improved and identified key observational needs for the functions of terrestrial ecosystems.

Table of Contents

List of Tables

List of Figures

CHAPTER 1: Introduction

1.1. Motivation and Objectives

Terrestrial ecosystems are the backbone of all life on Earth, and they provide the essential resources that people need. Everything we eat comes directly or indirectly from plants. Throughout human history, approximately 7,000 different plant species have been used as food because of their ability to store carbon and produce nutrition for people and animals. Plants also help regulate the water cycle by moving water from the soil to the atmosphere in what is, in reality, a purification process. The terrestrial ecosystem involved many complicated biogeochemical and biogeophysical processes. All these processes are influenced by atmospheric conditions, and they also give feedback to the climate. Past studies have shown that, in the near future, climate change is likely to increase global temperatures by at least 2 oC and to reduce precipitation significantly during the summer months compared to the amounts of precipitation that occurred from 1986 through 2005 (IPCC, 2014). Also, there is substantial evidence that climate change will result in the increased frequency and intensity of extreme events on the Earth, such as heat waves and droughts during the summer months (Perkins et al., 2012). In addition, intensification of the global hydrological cycle has been observed over the past few years (Gedney et al., 2014). Therefore, it is important to understand how all of these important climatic changes might interact with environmental conditions.

1.2. Research Focuses

1.2.1. Isoprene Emission under Drought

I am interested in studying isoprene emissions during drought conditions because this compound is produced by plants and is an important component in many reactions

that occur in the biosphere. Isoprene (2-methyl-1,3-butadiene, C5H8) is the second most abundant biogenic volatile organic compound (BVOC) in the terrestrial ecosystem. Its production on a global basis amounts to 570 Tg/year (Guenther et al., 1995), which is associated with carbon assimilation (Minson & Fall, 1989; Loreto & Sharkey, 1990; Lerdau et al., 1997; Guenther 2002). Thus, this compound offers great promise for productive studies of atmospheric chemistry (Houwelling et al., 1998; Greanier et al., 2000; Collins et al., 2002).

Regarding the response of isoprene emissions to drought, some leaf-level studies have suggested the isoprene is characterized by a protective action when deficits in water cause stress (Sharkey & Loreto, 1993; Fortunati et al., 2008). The emissions of this compound also have been found to have a different response to drought conditions than the emissions of CO2. Explanations for these phenomena are that the biosynthesis of isoprene is catalyzed by enzyme isoprene synthase (ISPS) (Schnitzler et al., 1996). The isoprene synthase protein is produced in the chloroplast, and roughly 80% of the carbon in the isoprene molecule is derived from newly-assimilated photosynthetic intermediates in unstressed plants. When drought conditions exist, the production of carbon via photosynthesis in plants decreases, but a shift to alternative sources of carbon can sustain the production of isoprene. (Funk et al., 2004). Isoprene also is considered to improve the thermotolerance of leaves, thereby protecting photosynthetic membranes, i.e., the thylacoids, from permanent damage during severe conditions (Penuelas et al., 2005; Sharkey and Singsaas, 1995; Velikova and Lereto, 2005).

To more reliably estimate isoprene emissions during drought, several sensitivity studies have quantified the contributions of the principal environmental variables (Guenther, 2006; Wiedinmyer et al., 2001). Temperature has been found to be the

primary driver of seasonal variations relative to other activity factors (Huang et al., 2015). Soil moisture has been identified as a key uncertainty and must be improved for better representations of water stress (Monson et al., 2012; Tawfik et al., 2012; Huang et al., 2015) since the frequency of drought stress is predicted to increase as a result of climate change (Field et al., 2012). Many studies have highlighted the importance of using realistic wilting-point data and threshold (Guenther et al., 2014; Seco et al., 2015). The values of the soil moisture factor are very sensitive to the threshold and wilting point.

In this study, the Emissions of Gases and Aerosols from Nature model (Guenther et al., 2006, 2012) was used to determine the roles of soil moisture and temperature in predicting isoprene emissions during drought.

1.2.2. Role of Semiarid/Arid ecosystem and SIF retrieved from satellite

The impetus for my study of the activity of plants in a semi-arid/arid ecosystem was their disproportional role in determining the inter-annual variability of the global carbon cycle. Semi-arid ecosystems provide an important contribution to the global dynamics of atmospheric carbon. Such ecosystems include areas that provide limited water for grass and other plants, e.g., areas such as grasslands, open shrublands, and savannas. The growth of plants in semi-arid areas is dependent largely on the availability of water over regions in which the annual precipitation is usually low and occurs mainly in a few months rather than year-round (Jung et al., 2011). Such high sensitivity to water stress makes the role of semi-arid regions very important in a warming climate. Although most previous studies have identified tropical forests as the main driver of global carbon uptake, several recent studies have shown that semi-arid regions, especially those within the Southern Hemisphere, can dominate the inter-annual variability of the global terrestrial carbon cycle (Rotenberg and Yakir, 2010; Bastos et al., 2013; Poulter et al.,

2014, Cleverly et al., 2016). A study using flux tower data over the southwestern part of the United States indicated that a semi-arid system could switch from a net sink of carbon to a net source when different levels of precipitation occur. However, the representation of photosynthesis in boreal forests by current modelling and observational methods is still challenging. Anav et al. (2015) suggested that there were urgent needs to improve observation-based datasets and to develop carbon cycle modeling. They contended that these needs existed because the available data and modeling approaches at that time were inadequate and too simplistic to correctly estimate present GPP and to quantify the future uptake of carbon dioxide by the world's vegetation. Thus, a better understanding of the intrinsic link between hydroclimatic variations and carbon sink-source dynamics over global semi-arid regions is an urgent need.

Sun-induced fluorescence (SIF) is an electromagnetic signal emitted by the chlorophyll of leaves. The first global retrievals of satellite-based SIF, which was accomplished in 2011 (Frankenberg et al., 2011; Joiner et al., 2011), showed potential for being a direct proxy for photosynthetic activity, and the SIF signal responds instantaneously to perturbations in environmental conditions, such as light and water stress (Flexas et al., 2002; Papageorgiou and Govindjee, 2014; Daumard et al., 2010; Porcar-Castell et al., 2014; Baker et al., 2008; Sun et al., 2015). Many seasonal scale studies have been conducted using SIF datasets. Strong positive seasonal correlations between SIF retrieved from GOSAT and GOME-2 and GPP from model simulations and flux tower estimates have been determined empirically for different biomes (Frankenberg et al., 2011; Guanter et al., 2012; Lee et al., 2013; Parazoo et al., 2013; Joiner et al., 2014; Walther et al., 2016). Yang et al. (2015) reported that there were high diurnal and seasonal correlations between satellite-based and ground-based SIF and tower GPP in

deciduous forests. Also, the first efforts to constrain model GPP with SIF brought remarkable results in that the adjusted GPP values and seasonalities were in closer agreement with the flux tower measurements (Guanter et al., 2014; Parazoo et al., 2014; Zhang et al., 2014). However, no seasonal analysis was conducted for Australia with SIF data. In this study, we used satellite measurements of sun-induced chlorophyll fluorescence (SIF) to exam the seasonality of vegetation in response to variations in water stress over arid and semi-arid regions of Australia, depicting the plant phenology across a variety of ecosystems (Joiner et al., 2014; Walter et al., 2016),

We used the SIF retrieval from the the Global Ozone Monitoring Experiment-2 (GOME-2) and Orbiting Carbon Observatory-2 (OCO-2) (Crisp et al., 2008) with continuous global coverage. GOME-2 measures in the red and near-infrared (NIR) spectral regions with a spectral resolution of ~ 0.5 nm and a pixel size of ~ 40 km x 80 km (40 km x 40 km for MetOp-A since July 2013). The relatively coarse spectral resolution of GOME-2 was compensated by its high radiometric sensitivity and wide spectral coverage. This observational scenario was completed by the first SIF data from the NASA-JPL OCO-2 mission (launched in July 2014) with high resolution spectra of the O2-A band (757-775 nm), which enabled the retrieval of far-red SIF. Potentially, it could yield more accurate estimates of SIF.

1.2.3. Natural and anthropogenic effects on ET dynamics.

I also extended my research scope to biogeophysical components to obtain a more thorough understanding of the terrestrial ecosystem. Terrestrial evapotranspiration (ET) is arguably the central component of the biogeophysical process and functions as a vital link between energy, water, and carbon cycles, so it has important implications for the availability and usage of fresh water resources by people and terrestrial ecosystems

(Seneviratne et al., 2006; Trenberth et al., 2009; Fisher et al., 2011; Wang and Dickinson, 2012).

Natural environmental factors (e.g., precipitation, temperature, incident solar radiation, soil moisture, wind and atmospheric teleconnections) regulate ET and its variability across different terrestrial ecosystems (Teuling et al., 2009; Jung et al., 2010; Wang et al., 2010; Vinukollu et al., 2011; Zhang et al., 2012; Miralles et al., 2014). These natural controls and limitations/co-limitations of ET are scale-dependent. Their mechanistic understanding is very important to predict the tendency and variability of ET (Wang and Dickinson, 2012). Changes in land use and land cover, in the withdrawal of ground water, and irrigation induced by people can directly alter the amount and timing of ET by modifying the local water and energy balances (Piao et al., 2007; Gerten, 2013; Leng et al., 2013, 2014a, 2014b; Lo and Famiglietti, 2013; Sterling et al., 2013; Lei et al., 2014c). People's activities that contribute to the emissions of greenhouse gases, the deposition of atmospheric nitrogen (NDE), and ozone pollution also can alter ET indirectly through changes in the physiological, structural, and compositional responses of plants (Gedney et al., 2006; Betts et al., 2007; Sitch et al., 2007; Cao et al., 2009; Leakey et al., 2009). Discriminating these anthropogenic perturbations from natural factors is expected to increase in importance as anthropogenic transformation of the Earth's systems becomes more pervasive (Seneviratne et al., 2010; Gerten, 2013).

To develop a better understanding of these differences in simulated ET patterns and the relative roles of the sensitivities and structures of the models, the experimental setup and boundary/initial data must be similar among the different models that are used. We leveraged the controlled factorial experiments and model simulation protocol from the Multi-Scale Synthesis and Terrestrial Model Intercomparison Project (MsTMIP)

(Huntzinger et al., 2013). Further, we synthesized a global ET time series (1982–2010) based on a diverse set of diagnostic ET products (Table 1) and on the methodology reported recently by Mueller et al. (2013). The partitioning of ET (e.g., canopy transpiration (Tr) and evaporation from wet canopy and bare soil (ET–Tr)) and the variation of those ET components are poorly understood and less constrained by observations (Lawrence et al., 2007; Jasechko et al., 2013; Swenson and Lawrence, 2014; Wang et al., 2014). The MsTMIP modeling framework advanced researchers' understanding of trends in ET by providing predictions of the individual ET components. Thus, in this study, we conducted further investigations of the contributions of individual influencing factors on the spatial and temporal characteristics of these ET constituents.

1.3. SCIENTIFIC QUESTIONS

The scientific questions addressed in this dissertation are:

(1) What are the relative contributions of temperature and soil moisture to the dynamic of isoprene? Can the model simulate the variations of isoprene emissions for different intensities and phases of droughts?

(2) Can the use of satellites to conduct remote sensing of solar-induced chlorophyll fluorescence (SIF) accurately represent the seasonal cycles of arid/semi-arid plants? Is SIF a better indicator of photosynthetic activity than other biomass variables?

(3) What are the roles of natural and anthropogenic factors on controlling global terrestrial evapotranspiration trends from 1982 to 2010?

To answer the above scientific questions, in Chapter 2, we used MEGAN2.1 embedded in CLM4.5 to develop an understanding of the roles of the moisture content and the temperature of soil, and we compared the results of the simulations with canopy-level flux data. In the discussion presented in Chapter 2, we provide insights for

improving the modeling of the response of isoprene emissions to drought conditions. Chapter 2 evaluates the capability of SIF to synchronize the plant activity by qualifying and quantifying its relationship with the availability of water. To answer the question (3) above, in Chapter 4 we leveraged the controlled factorial experiments and model simulation protocol from the Multi-Scale Synthesis and Terrestrial Model Intercomparison Project (MsTMIP). With the MsTMIP modeling framework, we analyzed the individual ET components and determined how the individual influencing factors impacted ET. In Chapter 5, our major findings are summarized and future directions are discussed.

CHAPTER 2: Disentangling the Roles of Soil Moisture and Air Temperature in Predicting Isoprene Emissions during Drought: A Case Study in a Temperate Forest in the Missouri Ozarks

2.1. ABSTRACT

Drought conditions strongly affect the emissions of biogenic volatile organic compounds (BVOCs). However, predicting BVOC emissions during such conditions is challenging because of the intermingled roles of water deficits and high air temperatures, which are the two main environmental stressors during droughts. In this study, we investigated changes in the emissions of isoprene, the second-most common BVOC in terrestrial ecosystems (after methane). Our investigation was conducted during two drought events that occurred at a given site in the Missouri Ozarks that had exhibited the highest, canopy-scale isoprene emissions reported to date for temperate deciduous forests. Our aim was to develop an understanding of the roles of these two stressors, i.e., water deficits and high temperatures, in predicting isoprene fluxes during drought. The two drought events we studied were a moderate drought event in 2011 and a severe drought event in 2012. We compared observations with simulations by a state-of-the-art land model coupled with the Model of Emissions of Gases and Aerosols from Nature version 2.1 (MEGAN2.1) during the different phases of the drought. The model captured the overall variations of the observed emissions for both events during the pre-drought phases when the temperature dominated the temporal dynamics of the isoprene emissions. However, after the pre-drought phase, there were substantial differences between our observations and the model's predictions of isoprene emissions. Specifically, our observations depicted a delayed response of isoprene fluxes to deficits of water in the soil, while the results from the model indicated that there was an immediate response to the onset of the drought. During the peak stress phase, especially that of the 2012 event,

isoprene emissions and the water content of the soil were observed to be strongly correlated, but no strong correlation was indicated by the model's predictions. We also tested the sensitivity of predicted isoprene emissions to various parameterization schemes for the controlling effect of soil water. Our results demonstrated that temperature and the water content of the soil water jointly controlled isoprene emission, but their relative effects were sensitive to the phases in the development of the drought. To determine the phase dependencies of the relative temperature/water stress effects during the drought, there was a need for more realistic model representations of the controls of biochemical and physiological processes (e.g., carbon substrate dynamics, isoprenoid synthesis, and the nonlinearity of plant water stress vs. the water deficit in the soil) on isoprene emission.

2.2. INTRODUCTION

Other than methane, isoprene is the most abundant volatile organic compound emitted from terrestrial ecosystems, with a global flux of approximately 400-600 TgCyear-1 (Ashworth et al., 2010; Guenther et al., 1995; Guenther et al., 2006; Müller et al., 2008; Arneth et al., 2008; Henrot et al., 2016). Isoprene emissions affect atmospheric chemistry by acting as a precursor of tropospheric ozone and by leading to the formation of secondary organic aerosols (Houweling et al., 1998; Granier et al, 2000; Hu et al., 2016; Collins et al., 2002). The magnitude of isoprene's effects depends on the biological properties of plant species and environmental factors (Monson et al., 2012; Tawfik et al., 2012; Monson et al., 1994; Arneth et al., 2011). For example, some oak trees are strong emitters of isoprene, and their emission rates can be as high as 53 mg m-2 h-1 (Seco et al., 2015; Geron et al., 2001; Wiedinmyer et al., 2005). Since the emissions from most needle-leaf deciduous trees are negligible (Guenther et al., 2012), this indicates a strong,

inter-species difference. Leaf phenology (e.g., Leaf Area Index, LAI) determines the amount of leaves that potentially can serve as emission units in a given plant, which, in turn, affects the seasonal variation in the isoprene emissions of deciduous plants (Tawfik et al., 2012; Kuhn et al., 2004; Huang et al., 2014; Gulden et al., 2007). Environmental factors, including temperature, light, the concentration of CO2, and the availability of water, affect plants' biological traits and strongly influence the rate of isoprene emissions (Guenther et al., 1993; Harley et al., 1996; Owen et al., 2002; Rodríguez-Calcerrada et al., 2012; Pétron et al., 2001; Sharkey et al., 1996; Rosenstiel et al., 2003; Pegoraro et al., 2004a; Wilkinson et al., 2009; Fortunati et al., 2008; Funk et al., 2004; Genard-Zielinski et al., 2014; Lathiere et al., 2010; Pegoraro et al., 20014b; Llusià et al., 2008). Among these factors, temperature and the availability of water are of particular importance because both of these factors regulate isoprene synthase activity (Lehning et al., 1999; Monson et al., 1992; Rasulov et al., 2010; Fall et al., 1998) and the supply of dimethylallyl diphosphate (DMADP) (Schnitzler et al., 2005; Sun et al., 2013; Li et al., 2011).

Isoprene emissions usually increase as the temperature increases up to 40 oC (Monson et al., 1992; Sanadze et al., 1966), depending on the plants' physiological constraints. Studies also have shown that temperature and CO2 concentration can interact and impact isoprene emissions, but the underlying mechanism is unresolved (Monson et al., 2012; Sun et al., 2013; Monson et al., 2016; Li et al., 2013; Potosnak et al., 2014a). There have been contradictory reports regarding the impact of the availability of water on isoprene emissions, and this availability ultimately depends on the supply of moisture in the soil. Peñuelas and Staudt (2010) reviewed previous studies concerning the relationship between isoprene emissions and water stress, and they indicated that about

50% of the studies reported decreased isoprene emissions due to water stress, and the rest reported increased emissions or no fundamental changes. Such discrepancies probably resulted from variations in the intensity and timing of the stress and from different species having different resistances to drought. Thus, the mechanisms that determine plants' responses to water stress are complicated. The rate of isoprene emissions is regulated by both the concentration of the DMADP substrate and the isoprene synthase activity (Rasulov et al., 2010; Wolfertz et al., 2004; Rasulov et al., 2009). Water stress can suppress the activity of an enzyme (ISPS), which catalyzes the conversion of DMADP into isoprene (Fortunati et al., 2008; Schnitzler et al., 2005). However, the increased temperature of the leaves, which is caused by reduced transpiration due to the closure of stomata due to water stress, may enhance the isoprene emission rate.

Understanding the relative effects of temperature and moisture in the soil on isoprene emissions is critical during drought because heat stress and water stress usually occur simultaneously, but they have counteracting impacts on isoprene emissions. However, their relative effects on isoprene emissions are difficult to determine based solely on observations. Several studies have quantified their individual and collective effects using models to predict isoprene emissions (Müller et al., 2008; Huang et al., 2015; Wiedinmyer et al., 2001). It has been reported that temperature, unlike other factors, primarily affects the seasonal variations in emissions (Müller et al., 2008; Tawfik et al., 2012; Huang et al., 2015; Stavrakou et al., 2014). The effect of the availability of water on isoprene emissions has been identified as a key source of uncertainty in predicting isoprene emissions during the stress of a drought (Monson et al., 2012; Tawfik et al., 2012; Huang et al., 2015). Since the frequency of drought is likely to increase with

climate change (IPCC, 2013), it is important to realistically represent the impact of drought on the future trajectory of isoprene emissions.

Our aim in this study was to separate the relative effects of temperature and moisture in the soil on isoprene emissions during drought. We investigated both in-situ measurements and state-of-art model simulations conducted for two drought events (one in 2011 and one in 2012) at the Missouri Ozarks Forest site (MOFLUX), a core AmeriFlux site (Gu et al., 2006, 2007, 2015). We chose the Model of Emissions of Gases and Aerosols from Nature, version 2.1 (MEGAN2.1) as our testbed, which has been incorporated into the National Center for Atmospheric Research's (NCAR's) Community Land Model version 4.5 (CLM4.5). CLM simulates the dynamics of the leaf temperature and soil moisture stress factors through its energy and water balance framework, providing direct environmental conditions that are needed as inputs to MEGAN for predicting isoprene emissions. Thus, the MEGAN/CLM coupling allows us to evaluate the performance of model representations of environmental stressors and better understand the separate and joint effects of these stressors on isoprene emissions.

2.3. METHOD

2.3.1. The Two Extreme Drought Events: A Comparative Case Study

In this paper, we report the results of our study of two drought events at MOFLUX in 2011 and 2012, with the former having moderate severity and the latter having extreme severity. This contrast between 2011 and 2012 provides a good opportunity to evaluate the response of isoprene emissions to soil moisture deficits and high temperatures during droughts of different severities. At the beginning of July 2011, hot and dry conditions started to spread across southwestern Missouri, affecting

vegetation activities (Potosnak et al., 2014b). Although cooler air occurred occasionally in Missouri, the dry conditions continued until October 2011. The 2012 drought event was one of the most severe in the past 25 years in Missouri (Gu et al., 2015). Water stress started to develop at the end of June 2012, and it reached the "extreme" category as defined by the U.S. Drought Monitor (USDM) in August 2012.

2.3.2. Site Characteristics and Measurements of Isoprene Emissions

The study site (MOFLUX) is located in the Baskett Wildlife Research and Education Area, Missouri, USA (38.7° N and 92.2° W; elevation = 219 m). MOFLUX is dominated by oak trees and is known as the "isoprene volcano" of the world (Wiedinmye et al., 2005), because it has the highest rate of isoprene emissions ever reported in the literature (53 mg m^{-2} h^{-1}) (Potosnak et al., 2014b). The site has two strong isoprene emitters, i.e., white oaks (Quercus alba L.) and red oaks (Q. velutina L.). To the best of our knowledge, it is the only site for which there have been whole canopy measurements of isoprene emissions during severe drought events. These features make MOFLUX one of the best sites in the world to perform our study. Previous studies at the same site reported discrepancies between the observed and model-predicted isoprene emissions at both the leaf level (Geron et al., 2016) and the canopy level (Geron et al., 2001; Potosnak et al., 2014b), but the relative roles of temperature and water deficit were not quantified.

At MOFLUX, the average height of the canopy is 20 m, and the average peak LAI is 3.7 during the growing season. There is a broad range of dominant soils at the site, and they are classified as "Steep Stony Land," a designation that includes all of the rocky slopes that have a thin covering of soil and Weller silt loam (fine, smectitic, mesic Aquertic Chromic Hapludalf) (Young et al., 2003; Garrett et al., 1973). The characteristics of the soils at the site potentially could exacerbate water stress during

periods of drought. The measurements of the isoprene flux were collected at a height of 29 m with a fast isoprene sensor in 2011 (Potosnak et al., 2014b) and with a Proton Transfer Reaction Mass Spectrometer (PTR-MS) (Karl et al., 2001) in 2012 (Seco et al., 2015). The volumetric water content of the soil was measured at several depths between 0 and 100 cm at time steps of 30 min. To monitor the dynamics of the effects of water stress and drought on the plants, the pre-dawn leaf water potential Ψ_{pd} was measured with a pressure chamber using leaf samples collected before dawn (Pallardy et al., 1991; Turner et al., 1981). The value of Ψ_{pd} is a reliable measure of the availability of water to the plants, and it is an integrated indicator of the plants' water stress. It has been found to explain the inter-annual variability in tree mortality at the MOFLUX site (Gu et al., 2015). Measurements of Ψ_{pd} were made either weekly or biweekly during the growing seasons from mid-May to late October (Pallardy et al., 2015; Yang et al., 2010; Belden et al., 2009). More details on the characteristics of the site and the associated measurements are provided elsewhere.

2.3.3. Model of Emissions of Gases and Aerosols from Nature (MEGAN)

The MEGAN model is a modeling parameterization to simulate BVOCs' fluxes emitted from a land system. It has been used extensively to estimate isoprene emissions from landscapes from regional to global scales. MEGAN has been coupled to various land surface models that produce dynamic simulations of the energy balance of the canopy and soils and of the water and carbon cycles. In this study, we used the NCAR community land model, version 4.5 (CLM4.5) and the land component of the Community Earth System Model (CESM) as a testbed (Oleson et al., 2010). In then following, we briefly describe the formulations of the models of isoprene emissions in the latest version of MEGAN, i.e., MEGAN 2.1. The details of the derivation of the model and the

parameters used can be found elsewhere (Guenther et al., 2006, 2012). In our case, the standard conditions were defined as an air temperature 29.9 ºC, a soil moisture of 0.3 mm^3mm^{-3}, solar elevation angle of 60º, and photosynthetic photon flux density (PPFD) of ~1500 $\mu molm^{-2}s^{-1}$ at the top of the canopy. More details can be found in citation (Guenther et al., 2006). The isoprene flux of a canopy in MEGAN2.1 is formulated as a product of two components, i.e., the basal emission rate and the emission activity factors that represent the regulation of environmental conditions and plant structural/physiological states:

$$F = \gamma \sum \varepsilon_i \chi_i, \tag{2.1}$$

where F is The emissions rate of isoprene from terrestrial landscapes, ε_i is the basal emission factor at standard environmental conditions for vegetation type i, χ_i is the corresponding fractional areal coverage, and γ is a composite emission activity factor that consists of several terms representing major processes that drive the variations in isoprene emissions. The equation for γ is:

$$\gamma = C_{CE} LAI \gamma_P \gamma_T \gamma_{age} \gamma_{SM} \gamma_C, \tag{2.2}$$

where γ_P is the light-dependent emission factor controlled by PPFD, γ_T is the temperature response of enzymatic activity, γ_{SM} is the soil moisture response, γ_{age} is the leaf age response, γ_C is the CO_2 response, and LAI is the leaf area index. C_{CE} is defined as the canopy environment coefficient and, herein, it is assigned the constant value of 0.3, which normalizes γ to 1 at standard conditions (Guenther et al., 2012). The value of C_{CE} depends on the canopy model that MEGAN is coupled with, and we used CLM. A different canopy model would require the use of a different C_{CE}.

Specifically, the temperature activity factor, γ_T, is calculated as:

$$\gamma_T = E_{opt}[C_{T2} exp\ (C_{T1}X)/(C_{T2} - C_{T1}(1 - exp\ (C_{T2}X)))], \tag{2.3}$$

where E_{opt} is the maximum normalized emission capacity at the optimal temperature T_{opt}, C_{CE} = 95, and C_{CE} = 230) are empirical coefficients, and X is expressed as:

$$X = [\frac{1}{T_{opt}} - \frac{1}{T}]/0.00831, \quad (2.4)$$

where T is the leaf temperature, simulated by CLM, and details on the calculation of T_{opt} can be found in (Guenther et al., 2006).

The soil moisture activity factor is computed as:

$$\gamma_{SM} = \sum_{i=1}^{N_{root}} r_i \, max\,(0, min\,(1,\ (\theta_i - \theta_i^w)/\Delta\theta_1)), \quad (2.5)$$

where θ_i is the volumetric water content ($mm^3 mm^{-3}$), θ_i^w is the wilting point (a water content threshold below which plants wilt), and $\Delta\theta_1$ is an empirical parameter (0.06) (Pegoraro et al., 2004a). Both θ_i and θ_i^w are soil-layer specific and simulated by CLM. The soil moisture activity factor is calculated as a weighted sum by root fractions (r_i) across all soil layers (with N_{root} = 10 layers), which are 286 cm deep (Oleson et al., 2010). MEGAN2.1 uses this formulation to represent soil moisture stress in the range from zero (soil moisture fully depleted) to one (no water stress).

To examine the sensitivity of soil moisture activity factor on modeled isoprene emissions, we tested two additional formulations of the soil moisture function along with the default MEGAN2.1 formulation defined in Equation 2.5. First, we tested the soil moisture stress factor used in CLM, denoted as β_{CLM}, which is used to down-regulate photosynthesis and stomatal conductance under water stress. The term β_{CLM} is calculated as:

$$\beta_{CLM} = \sum_{i=1}^{N_{root}} r_i min\,(1.0,\ (\Psi_c - \Psi_i)/(\Psi_c - \Psi_o)), \quad (2.6)$$

where Ψ_i is the soil water matric potential (mm), and Ψ_o and Ψ_c are the soil water potentials (mm) at which the leaf stomata are fully open and fully closed, respectively. Equation 2.6 indicates that β_{CLM} follows a similar format as γ_{SM}, but it uses the water

matric potential rather than the volume content used in MEGAN to calculate the soil moisture activity factor.

In the second test, we used the soil moisture stress factor from the Simple Biosphere model (SiB) (Xue et al., 1991):

$$\beta_{SiB} = \sum_{i=1}^{N_{root}} r_i min\,(1.0, 1.0 - e^{-c_2 \ln(\Psi_{wilt}/\Psi_i)}), \quad (2.7)$$

where Ψ_{wilt} is the soil water potential at the wilting point, and c_2 is a slope factor that is equal to 5.57 for the broadleaf deciduous trees in MOFLUX (Xue et al., 1991).

All three soil moisture factors range from zero to one, but they have different functional shapes with SWC (soil water content) (Figure 2.1). The MEGAN formulation, γ_{SM}, increases linearly with SWC, while β_{CLM} and β_{SiB} have non-linear relationships with SWC. In particular, β_{SiB} (and β_{CLM} to a lesser extent) decreases rapidly when SWC is low. In this sensitivity test, we replaced γ_{SM} with β_{CLM} or β_{SiB} to investigate the effect on the modeled isoprene emissions.

2.3.4. Model Simulation Experiments

In this study, we ran MEGAN/CLM simulations at MOFLUX in the offline mode, driven by observed meteorological datasets (air temperature, shortwave and longwave radiation, relative humidity, precipitation, and wind speed). Other site-specific information used included seasonally-varying, measured LAI, temperate broadleaf deciduous forest as the plant functional type, and soil texture was 55% sand, 40% silt, and 5% clay. Hydrology calculations were conducted with 10 soil layers, and they depended on the root distribution of the PFT (plant functional type), as in standard CLM simulations. With these meteorological-forcing and site-specific parameters, CLM4.5 simulated the leaf temperature and SWC, which were used as inputs to MEGAN to predict isoprene emissions. We performed a 50-year spin-up simulation to ensure that the

soil moisture reached equilibrium. The spin-up simulation was driven by observed meteorological data from 2011. Then, we ran the actual model simulations for 2011 and 2012 at a time step of 0.5 hr, consistent with the measured isoprene flux emissions. Four different model simulations were performed for comparison with observations (Table 2.1). The first simulation (denoted as MOD_γ_{SM}) used the default soil moisture factor in MEGAN, the second (denoted as MOD_β_{CLM}) replaced the default soil moisture factor with the CLM formulation, and the third (denoted as MOD_β_{SiB}) replaced the default soil moisture factor with the SiB formulation. We performed a fourth simulation (denoted as MOD_*SWCobs*), which replaced the CLM-simulated SWC with the observed SWC at MOFLUX and the wilting point parameter θ_i^w (Equation 2.4) with a value of 0.23 mm^3mm^{-3}, a site-specific value suggested by Seco et al. (2015). The purpose of performing the last simulation was to investigate the impact of bias in soil moisture simulated by CLM on predicted isoprene emissions. This impact is in addition to that of the bias that resulted from the parameterization of the soil moisture activity factor. The potential bias in simulated soil moisture may come from both "process" and "parameter" errors in the calculation of soil moisture (Du et al., 2016).

2.3.4. Data Analysis Framework

In our analysis, we divided each individual drought event into four phases, i.e., pre-drought, developing, peak stress, and post-drought. Here, the seasonal pattern of predawn leaf water potential (Ψ_{pd}) was used to identify the different phases of the drought. In 2011, the pre-drought phase was identified to be the time before Ψ_{pd} dropped rapidly to -0.5 MPa. The developing phase occurred with -1.4 MPa < Ψ_{pd} < -0.5 MPa. The peak phase occurred when Ψ_{pd} < -1.4 MPa. The post-drought phase was identified when Ψ_{pd} recovered to above-0.5 MPa. The temporal dynamics of Ψ_{pd} in 2011 showed

that the drought started at the end of July, peaked around mid-September, and ended one month later. We did not include the post-drought phase of 2011 in our analysis because the growing season ended before Ψ_{pd} recovered (Figure 2.2). In 2012, the seasonal pattern of Ψ_{pd} showed a pre-drought phase of $\Psi_{pd} > -0.7$ MPa, a developing phase of $-2.5 < \Psi_{pd} < -0.7$ MPa, a peak phase of $\Psi_{pd} < -2.5$ MPa, and a post-drought phase when Ψ_{pd} returned to above -0.7 MPa. The 2012 drought event was more severe and peaked earlier than that of 2011. We used Ψ_{pd} instead of soil moisture to determine drought phases because Ψ_{pd} directly tracks the status of the plants' water. Note that corresponding drought phases had different ranges of Ψ_{pd} in 2011 and 2012 because the droughts in these two years had markedly different severities. Using the same Ψ_{pd} threshold values for 2011 and 2012 would result in some periods clearly misidentified for their stages in the drought development process. For the purpose of this study, it is important to clarify the impact of drought phase development on isoprene emissions modeling, which justifies the use of different ranges of Ψ_{pd} for 2011 and 2012.

We analyzed the relative effects of temperature and soil moisture for each drought phase. We chose air temperature instead of leaf temperature in our study to correlate with isoprene emissions because 1) leaf temperature, although it directly regulates the emission fluxes, is not directly observable, and, hence, it is difficult to compare with model simulations and 2) leaf temperature depends ultimately on air temperature and, thus, is highly correlated with air temperature on scales from diurnal to seasonal; therefore, air temperature can serve as a good proxy for leaf temperature. In the following texts, we use "temperature" to refer to air temperature unless specified otherwise.

To quantify the relationship between isoprene emissions and temperature/soil moisture, we computed both the Pearson correlation coefficient and the partial correlation

coefficient. The former is a linear correlation between two variables of interest, while the latter quantifies the linkage between the dependent and independent variables when multiple independent variables are involved. In our case, the partial correlation coefficient can quantify the coupling between isoprene emissions and temperature (or SWC) by removing the impact of SWC (or temperature). Then, we computed the student's-t value to test the significance of the correlation coefficient. The paired datasets also were fitted to a linear least squares model. We calculated and plotted the regression lines if the regressions passed the 0.05 significance test (p-value < 0.05).

2.4. RESULTS

Our results show that the observed and simulated isoprene emissions were in good agreement and both increased with increasing temperature during the pre-drought phase for both 2011 and 2012 (Figure 2.1). In this pre-drought phase, there was sufficient water supply, and, hence, the value of the soil moisture activity factor remained at one, indicating that plant growth was not limited by the water supply. The observation-model agreement held for all simulation experiments regardless of the different formulations of soil moisture activity factor. However, modeled predictions of isoprene emissions diverged from each other and from the observation two weeks after the onset of the drought (i.e., the developing phase). For example, the default model (MOD_ γ_{SM}) simulated decreased emissions following the sudden decrease in Ψ_{pd} and soil moisture in 2011, while the observed emissions continued to increase with increasing temperature in the earlier stage of the developing phase. MOD_*SWCobs* did a good job of tracking the initial increase in emissions that were observed, but it underestimated the emissions as compared to observation. In 2012, the MOD_γ_{SM} generally underestimated the isoprene emissions two weeks after the drought progressed into the developing phase, but it

captured the observed isoprene emission variations reasonably well. However, MOD_*SWCobs* overestimated the emissions throughout the peak phases.

These highly dynamic responses of predicted isoprene emissions to soil moisture motivated us to further quantify their relationships in a broader context (Figure 2.3 and Table 2.2). Here, we focused only on the event in 2012 because we had limited observational data for the peak drought phase in 2011. We found that, in the default MEGAN simulations, temperature dominated over soil moisture in controlling the model's prediction of isoprene emissions for all drought phases (Table 2.2). In contrast, observed emissions were controlled primarily by soil moisture as opposed to temperature in the peak stress and post-drought phases, and they even were affected adversely by soil moisture in the pre-phase and the developing phase (a negative correlation coefficient). The partial correlation coefficients revealed a similar pattern (Table 2.2) despite an elevated emission-SWC correlation in the model simulations. These results suggest that MEGAN tends to overestimate the dependency of isoprene emissions on temperature and to underestimate the dependency on soil water content during drought, especially when soil moisture is severely depleted.

The linear regression analysis shows positive slopes of observed isoprene emissions against SWC in both the peak-drought and post-drought phases, but it shows a negative slope in the pre-drought phase (Figure 2.3). In contrast, model-predicted isoprene emissions had a negative regression slope with SWC in the peak-drought phase and a positive slope in the post-drought phase. Such patterns hold with SWC at both 10 cm and 100 cm, despite the different absolute magnitudes of SWC at these two depths. This indicated that the observation-model discrepancy did not result from the depths of SWC used to perform the regression analysis. Thus, we proposed and tested two

hypotheses that may potentially explain the observation-model discrepancy, i.e., (1) the bias in simulated soil moisture itself by CLM and (2) the MEGAN formulations of the soil moisture activity factor that regulates isoprene emissions. To test the first hypothesis, we compared the emission-SWC relationships between MOD_γ_{SM} and MOD_*SWCobs* since the latter experiment used the observed SWC, excluding potential CLM bias in simulating SWC. We found that MOD_*SWCobs* produced a positive regression slope of isoprene emissions against SWC in the peak-drought phase (Figure 2.4a, Figure 2.4b), in agreement with observations (Figure 2.3a, Figure 2.3c) but in contrast with the default MEGAN/CLM simulations. This difference indicated that the soil moisture bias would contribute to the observation-model discrepancy in the soil moisture control on isoprene emissions. However, removal of soil moisture bias in the MEGAN simulation does not reverse the relative role between temperature and SWC as predicted by the default MEGAN simulation (Table 2.3). This each of reversal implies that the formulations of soil moisture activity factor also may have contributed to the observation-model discrepancy, motivating us to test the second hypothesis by performing a sensitivity test with different soil moisture activity factors (Table 2.3). We found that the relative effects of temperature and SWC on the prediction of isoprene emissions generally varied in the opposite direction in different simulation experiments, i.e., the partial correlation coefficient R of emission-temperature decreased while that of emission-SWC increased from MOD_ γ_{SM}, to MOD_β_{CLM} and MOD_β_{SiB}. Among all of the experiments, the default MEGAN simulation showed the closest R as compared to observations. This can be explained by the linear shape of γ_{SM} (Figure 2.1), which produces a steady response of soil moisture activity factor to SWC in the range of ~ 0.18-0.2 mm^3mm^{-3}, a typical range

in the peak-drought phase (Figure 2.2). The β_{CLM} and β_{SiB}, however, tended to saturate faster than γ_{SM} in this SWC range.

As mentioned above, we used air temperature as a proxy for leaf temperature, which directly controls isoprene emissions, because the latter is not directly observable at MOFLUX. We leveraged the model simulations to examine whether the use of air temperature would lead to any potential bias in the emission-temperature relationship (Figure 2.4c, Figure 2.4d). Our analysis showed that the relationship was very similar between air temperature and leaf temperature, indicating that the use of air temperature can well serve our purpose of isolating the roles of temperature from SWC. Note that this analysis relied on MOD_*SWCobs*, and hence the potential effect of simulated SWC bias was avoided.

2.5. DISCUSSIONS

Our study highlights the need for a more realistic model representation of dynamic isoprene emissions under various drought development phases. Even though the MEGAN model can simulate seasonal variation in isoprene fluxes reasonably well under normal conditions, it deviates from observations when the water supply is depleted. The current model tends to overestimate the control of temperature during a drought when heat stress also occurs. We showed that temperature may dominate the emission rate when water supply is not limiting, but its role diminishes when a severe water deficit constraint is present. Similar results were obtained for the leaf-level measurements of isoprene in 2012 at the same site (Geron et al., 2015). Our study, building on previous studies, separated the relative roles of temperature (stimulating the emissions) and soil moisture (suppressing the emissions) on the phases of drought development.

Our experiments cannot exclude the possibilities of the presence of other unrealistic model parameterizations that may be adjusted to improve the models' performance. Similarly, there may be other forms of soil moisture factor that work better. Nevertheless, the results obtained in this study made us wonder whether it is adequate to simply represent the soil moisture effect on isoprene emissions as a single factor that varies monotonically between 0 and 1. We believe our analysis highlights the urgency of developing an improved model representation of the influence of soil moisture on isoprene emissions. An explicit soil-to-leaf mechanistic basis of drought-induced stress might be a better solution (Xu et al., 2016; Fisher et al., 2006, 2007; Sperry et al., 1998). Potosnak et al. (2014b) suggested leaf temperature could be the key to understanding the response of isoprene emissions to drought. Leaf temperature directly regulates isoprene emissions because it depends on the supply of water in the soil and influences stomatal conductance. Potosnak et al. (2014b) determined a time-dependent response of isoprene emissions to drought, which, according to them, could not be explained by the MEGAN algorithm, and they suggested that isoprene emission should be decoupled with photosynthesis rather than sharing a similar water stress factor. During the beginning phase of a drought, the continuing increase of isoprene emissions was observed while photosynthesis started to decrease (Wu et al., 2015; Dani et al., 2014). Currently, there is no mechanism in the MEGAN model for considering this phenomenon because the process is complicated and remains unclear. Recent studies (Arab et al., 2016; Yuan et al., 2016) attributed the continuing increase during minor drought to the decrease in oxidative stress. Some mechanistic models also have been developed to investigate the effect of drought on isoprene emissions (Dani et al., 2014; Grote et al., 2014). A conceptual algorithm was proposed by Potosnak (2014b) in which low soil moisture led

to low photosynthesis, which increases leaf temperature. Isoprene emissions can continue for a period of time by using stored carbon. But as the drought continues, the carbon reserves are depleted, and isoprene emissions decrease. The conceptual model describes an increase of isoprene emissions at the beginning for a week, after which a decrease occurs. In addition, Grote el al. (2014) and Dani et al. (2014) demonstrated mechanistic models that partition plant absorbed energy between photosynthesis and isoprenoid synthesis. The models can well represent the effects of stomatal closure on isoprene emissions by coupling with the photosynthetic rate. Therefore, to better represent the drought effect, leaf physiological variables should be incorporated in the models in addition to soil variables. Also, some studies (Geron et al., 2016) have shown that atmospheric conditions have significantly different impacts on different plant species, and it's necessary to investigate species-specific feedback between plants and the atmosphere. They suggested that more species-level studies are needed in addition to canopy level. As such, additional mechanisms in desiccation tolerance should be included in the model algorithm. Therefore, a model that includes more realistic biochemical processes and biophysical processes during drought also should be developed.

2.6. CONCLUSIONS

We examined the separate effects of temperature and soil water content on isoprene emissions at the MOFLUX site during two drought events in 2011 and 2012. We compared observation data and the MEGAN model simulation coupled with CLM 4.5 in different phases of drought development. We found that temperature was a dominant factor under normal conditions without water stress. However, during a severe water deficit, exemplified by the peak stress phase, the impact of soil moisture on isoprene emissions was more critical than the impact of temperature. Model simulations

gave reasonably good isoprene emission predictions compared to observations under non-stress conditions, but they deviated from observations when soil moisture was severely depleted. The discrepancies between model results and observations during different drought phases suggest that the mechanisms through which soil moisture and temperature affect isoprene emission during drought are not well represented in the isoprene emission model, which is overly sensitive to temperature variations. A more process-based, time-dependent algorithm is required to realistically interpret environmental impacts on isoprene emissions for different drought intensities and development phases.

Simulation	Description
MOD_γ_{SM}	Simulation with the default soil moisture stress factor in MEGAN
MOD_β_{CLM}	Simulation with the soil moisture stress factor β_{CLM} in CLM
MOD_β_{SiB}	Simulation with the soil moisture stress factor β_{SiB} in SiB
MOD_*SWCobs*	Same as MOD_γ_{SM} except that the CLM-simulated SWC was replaced with the measured SWC and the observed wilting point parameter θ_i^w

Table 2.1. Descriptions of the simulations

	R				**$R_{partial}$**			
	OBS		**MODEL**		**OBS**		**MODEL**	
	SWC	**TEMP**	**SWC**	**TEMP**	**SWC**	**TEMP**	**SWC**	**TEMP**
Pre-drought	-0.50*	0.62*	-0.04	0.83*	-0.34	0.52*	0.15	0.83*
Developing	-0.14	0.43*	0.03	0.45*	0.14	0.43	0.55*	0.67*
Peak stress	0.81*	0.56*	-0.36*	0.84*	0.71*	0.14	0.61*	0.89*
Post-drought	0.60*	0.33	0.54*	0.88*	0.53*	-0.06	0.51*	0.87*

R: correlation coefficient; Rpartial: partial correlation coefficient; * p-value < 0.05

Table 2.2. Correlation analysis for isoprene emissions (MOD_ γ_{SM}) and environmental variables

	$R_{partial}$							
	MOD_ γ_{SM}		MOD_β_{CLM}		MOD_β_{SiB}		MOD_*SWCobs*	
	SWC	**TEMP**	**SWC**	**TEMP**	**SWC**	**TEMP**	**SWC**	**TEMP**
Pre-drought	0.15	0.83*	0.16	0.83*	0.03	0.90*	0.12	0.87*
Developing	0.55*	0.67*	0.40*	0.70*	0.19	0.84*	0.57*	0.88*
Peak stress	0.61*	0.89*	0.52*	0.87*	0.32*	0.83*	0.46*	0.88*
Post-drought	0.51*	0.87*	0.44*	0.87*	0.07	0.88*	0.65*	0.83*

* p-value < 0.05

Table 2.3. Partial correlation analysis for isoprene emissions and environmental variables

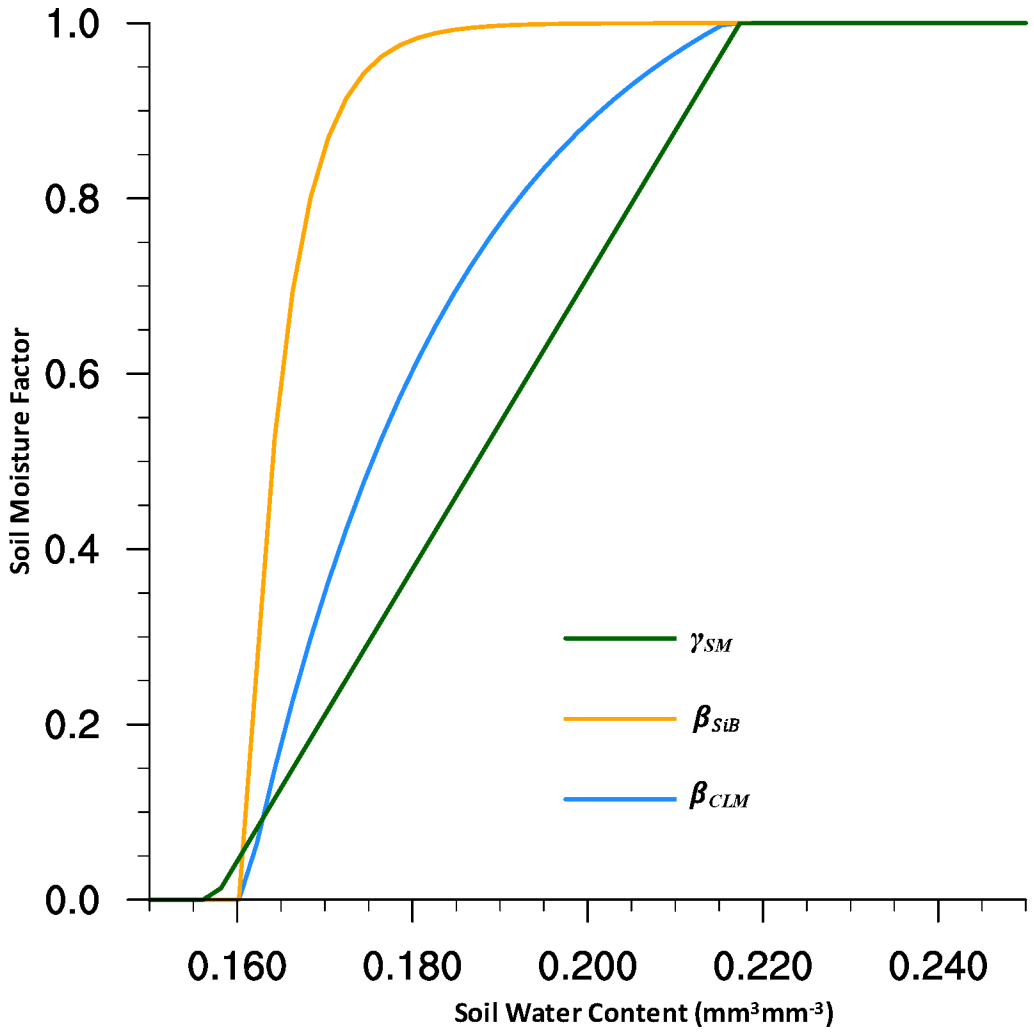

Figure 2.1. Sensitivity of isoprene emissions to different soil moisture factors. The model simulations used three different soil moisture factor candidates, i.e., the default MEGAN soil moisture activity factor (γ_{SM}), the CLM soil stress factor (β_{CLM}), and the SiB model soil stress factor (β_{SiB}). All factors are scaling factors from 0 to 1.

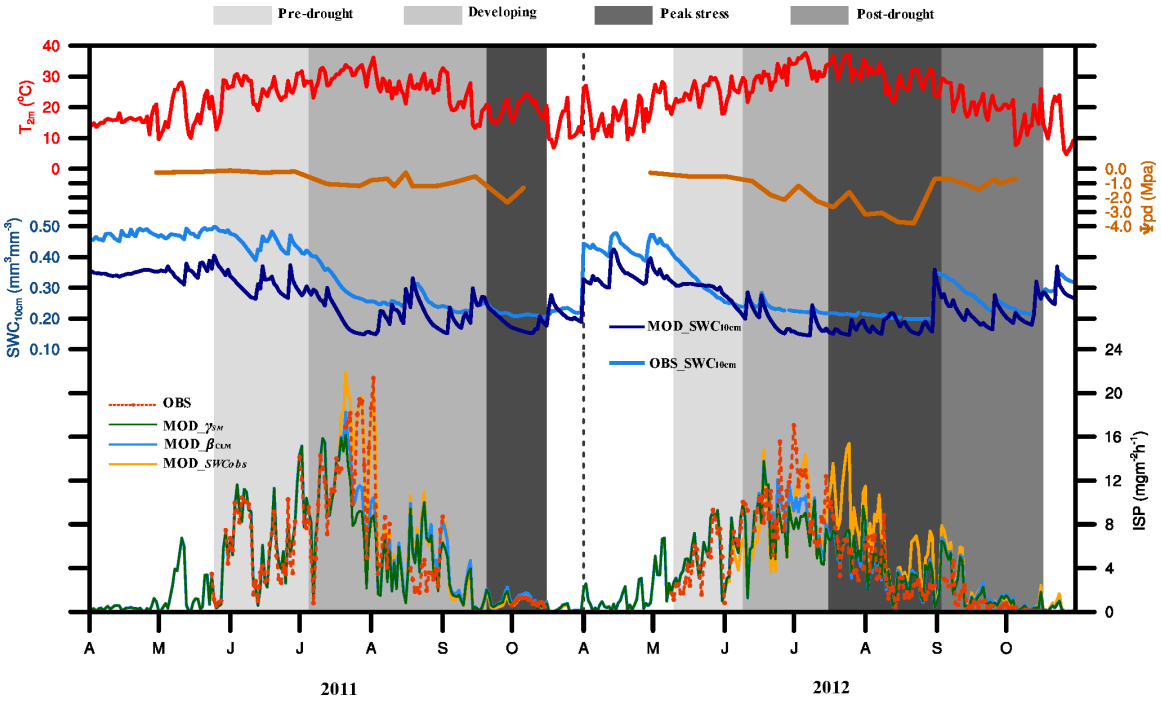

Figure 2.2. Time series of daytime average of environmental variables and isoprene emissions. Fig 2 includes the observed 2-meter air temperature (T_{2m}, red); observed and model simulated 10 cm soil water content (denoted as OBS_SWC_{10cm} and MOD_SWC_{10cm}, respectively, daytime average from 6:30 A.M. to 18:30 P.M.), and predawn leaf water potential (Ψ_{pd}) for 2011 and 2012 at the MOFLUX site. The bottom panel shows the comparison between observed and modeled isoprene emissions. Three model simulations were performed with different soil moisture factors, i.e., the default MEGAN soil moisture activity factor (denoted as MOD_γ_{SM}), the CLM formulation of soil moisture factor (MOD_β_{CLM}), the MEGAN factor with a site-specific wilting point (0.23 mm^3mm^{-3}) and soil water content from observations (denoted as *MOD_SWCobs*). The last simulation used observed soil moisture, while the first two took advantage of the CLM prediction of soil moisture. All soil moisture activity factors were on a scale from 0 to 1. Different drought phases are marked with different grey scales, including the pre-drought phase, the developing phase, the peak stress phase, and the post-drought phase.

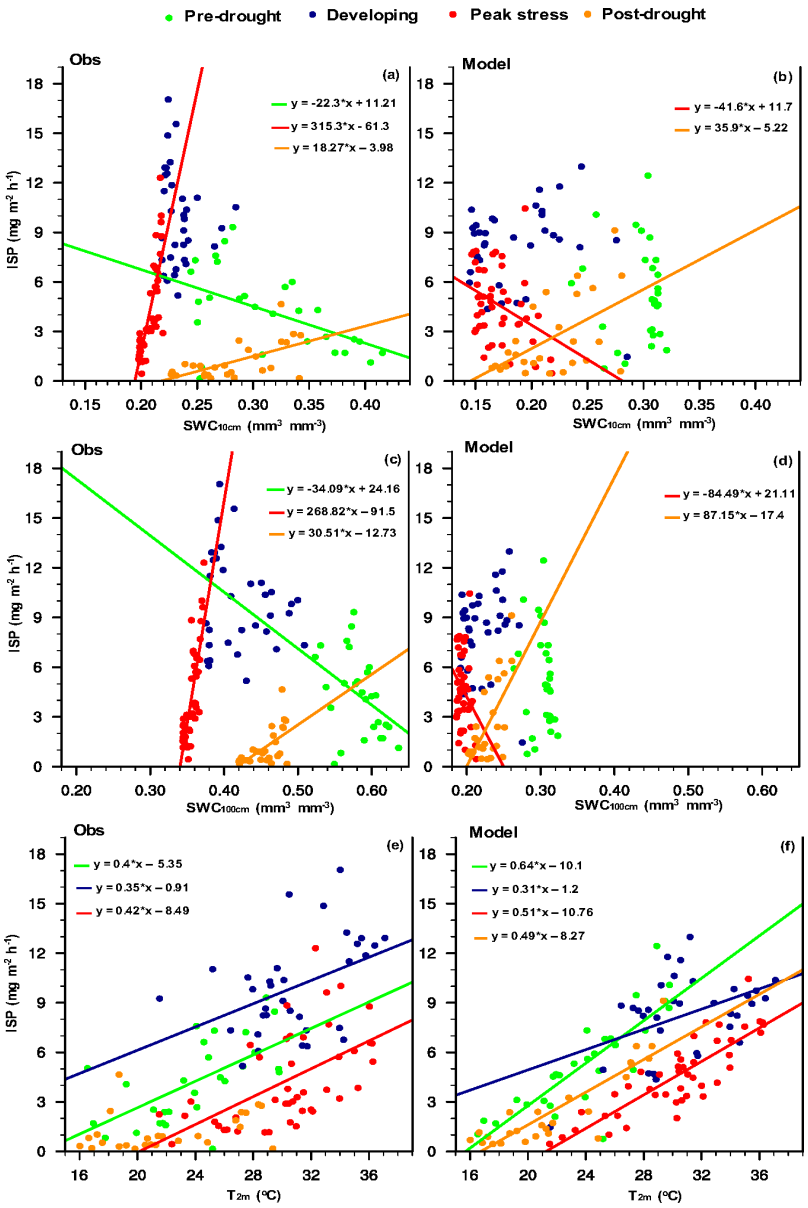

Figure 2.3. Regression analysis for isoprene emissions and environmental variables. Relationships of the isoprene emission (ISP) versus the water content of 10 cm of soil (SWC_{10cm}) (a), (b); water content of 100 cm of soil (SWC_{100cm}) (c) (d); 2m air temperature (T_{2m}) (e), (f); at individual drought phases for year 2012. (a), (c), (e) are observations, and (b), (d), (f) are model predictions from default MEGAN soil moisture formulation (MOD_γ_{SM}). Each scatter represents one single daytime-average value. The linear regression line information is shown if it passes the 0.05 significance test (p-value < 0.05).

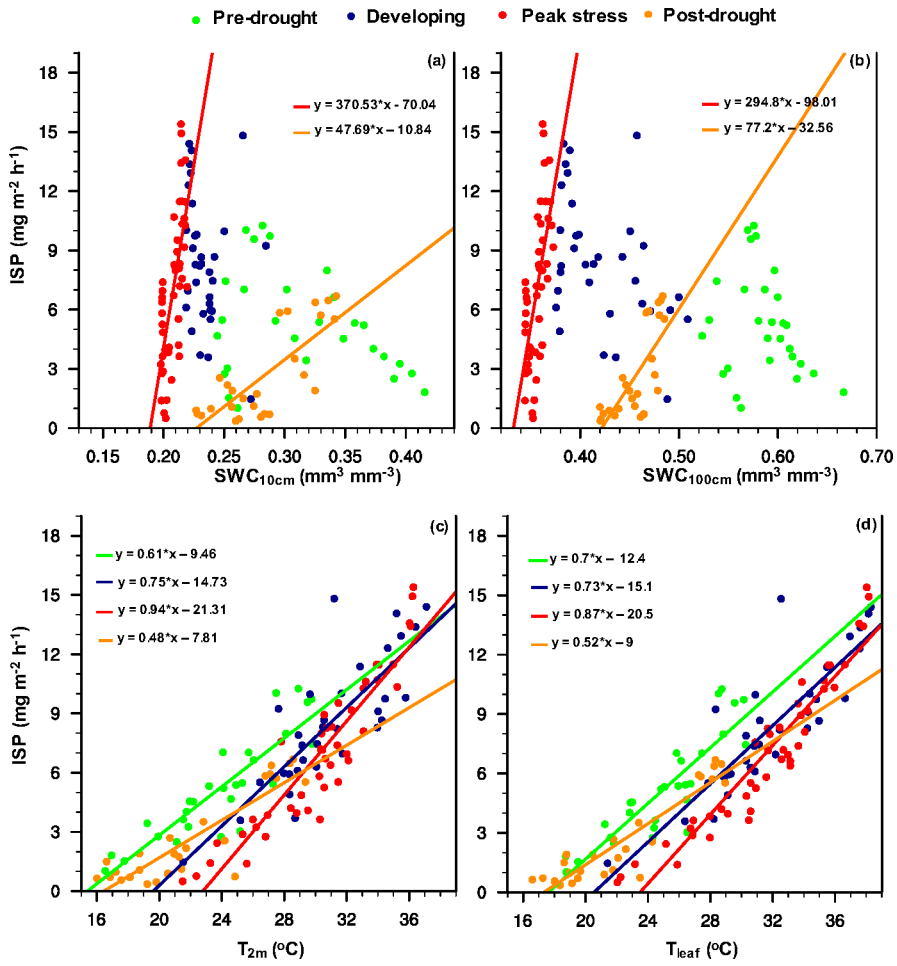

Figure 2.4. Regression analysis for isoprene emissions (MOD_*SWCobs*) and environmental variables Relationships of the isoprene emission (ISP) versus 10-cm soil water content (SWC_{10cm}) (a), 100-cm soil water content (SWC_{100cm}) (b), 2-m air temperature T_{2m} (c), or leaf temperature T_{leaf} (d). The isoprene emissions are model predictions from default MEGAN soil moisture formulation with measured SWC (MOD_*SWCobs*). Each scatter represents one single daytime-average value. The linear regression line is shown if it passes the 0.05 significance test (p-value < 0.05).

CHAPTER 3: The seasonality of dryland plants over Australia as revealed by satellite chlorophyll fluorescence

3.1. ABSTRACT

Arid and semi-arid ecosystems have critical roles in global terrestrial carbon cycling, but, currently, it is still challenging to observe and model photosynthesis in dry areas. In particular, the applicability of existing, satellite-based proxies of greenness to indicate photosynthetic activity is hindered by the weak signals emitted by sparse vegetation and by the confounding background effects. As an alternative, satellite measurements of solar-induced chlorophyll fluorescence (SIF) can be used as a direct proxy of photosynthetic activity. In this study, the sensitivity of the functioning of arid/semi-arid plants to water stress was analyzed using space-borne SIF measurements retrieved from the GOME-2 and OCO-2 instrument, and the results were compared to the Enhanced Vegetation Index (EVI), the Normalized Difference Vegetation Index (NDVI), and the Gross Primary Production (GPP) derived from MODIS data. We found that SIF and precipitation had similar spatial and seasonal variability in the arid and semi-arid regions in Australia. However, there were lags in the correlations between vegetation indices and precipitation. Our results demonstrated that space-borne SIF measurements are sensitive to water availability and capable of detecting rapid responses of plant activity in arid and semi-arid ecosystems.

3.2. INTRODUCTION

Arid and semi-arid ecosystems contribute to the dynamics associated with global atmospheric carbon. These ecosystems include grasslands, open shrublands, and savannas (Cherwin et al., 2012; Ponce-Campos et al., 2013; Moran et al., 2014; Ma et al., 2015; Scott et al., 2015). The growth of arid and semi-arid plants over the regions that usually

have low amounts of annual precipitation depends significantly on the availability of water, and their growth only occurs during a few months of the year (Jung et al., 2011). Such high sensitivity to water stress makes the arid and semi-arid regions especially vulnerable to the adverse effects of global warming (Yi et al., 2014; Huang et al., 2016). Although most previous studies identified tropical forests as vitally important for global carbon uptake, several recent studies have shown that semi-arid regions, especially those within the Southern Hemisphere, can dominate the inter-annual variability of the global terrestrial carbon cycle (Rotenberg and Yakir, 2010; Bastos et al., 2013; Poulter et al., 2014, Cleverly et al., 2016). A study using flux tower data over the southwest United States indicated that a semi-arid system could switch from a net sink to a net source of carbon during different precipitation levels (Scott et al., 2015). There is an urgent need to improve observation-based datasets and to develop carbon cycle models to correctly estimate the current GPP and to better quantify the future uptake of carbon dioxide by the world's vegetation (Anav et al., 2015). In particular, better information about the intrinsic link between hydroclimatic variations and carbon sink-source dynamics over global semi-arid regions is urgently needed. In this study, we focused on an important semi-arid region, Australia, because it impacts the global carbon cycle and also experiences the largest climate variability among the continents (Poulter et al., 2014; Ahlström et al., 2015). We performed seasonal scale analyses to investigate how Australia's semi-arid ecosystems respond to variable levels of precipitation with the aim of detecting rapid responses by the activities of plants in these systems.

Flux towers and remote sensing commonly are used for monitoring vegetation. The Australian and New Zealand flux tower network (OzFlux) provides important information, such as canopy-level CO_2 flux data and a small amount of images with

phnocams. In Australia, despite the dominance of deserts and xeric shrublands (49%) and the overwhelming importance of arid/semi-arid ecosystems (74%), only a small fraction of the OzFlux sites (two towers, 8% of the network) are located in these regions (Beringer et al., 2016). Vegetation information can be derived from satellite remote sensing imagery to achieve broad coverage of land areas. Satellite data provide spatially explicit time series of vegetation indexes (VI). VI typically are a function of reflectance in the red (R) and near-infrared (NIR), for example, Normalized Difference Vegetation Index NDVI = (NIR-R)/(NIR+R). The Enhanced Vegetation Index (EVI) in many ways is similar to NDVI, but it includes a term that eliminates the atmospheric effects of aerosols released during the burning of biomass (Huete et al., 2002). The difference in reflectance in R and NIR differentiates green vegetation from soil and non-photosynthetic vegetation. At the canopy level, the EVI has a linear relationship with the fraction of absorbed, photosynthetically-active radiation (fAPAR), which should be directly related to the photosynthetic capacity of the canopy. However, sometimes the relationship between vegetation and EVI can be confounded by soil reflectivity in sparse canopies, such as open shrub over semi-arid eco-regions (Huete et al., 1997; Gilabert et al., 2000; Asner et al., 2004; Dawelbait and Morari, 2011). The rareness of ground-truth observations and the uncertainty in greenness indexes call for new techniques to monitor the characteristics of vegetation more accurately.

Solar-induced fluorescence (SIF), emitted by the chlorophyll of leaves exposed to sunlight, is an optical signal emanating from the core of the photosynthetic machinery. Although active fluorescence has been used for decades to probe photosynthesis *in vivo* at the tissue and leaf scales (Papageorgiou and Govindjee, 2014; Porcar-Castell et al., 2014; Baker et al., 2008), passive SIF from instruments in space only became available

recently. Since the first global retrieval of satellite-based SIF (Frankenberg et al., 2011; Joiner et al., 2011; Guanter et al., 2012), SIF has been shown to be highly correlated with gross primary productivity across variance temporal and spatial scales (Frankenberg et al., 2011; Guanter et al., 2012; Lee et al., 2013; Parazoo et al., 2013; Joiner et al., 2014; Walther et al., 2016). For example, strong positive correlations between SIF retrieved from GOSAT and GOME-2 and GPP from model simulations and flux tower estimates have been found empirically for different biomes (Frankenberg et al., 2011; Guanter et al., 2012; Lee et al., 2013; Parazoo et al., 2013; Joiner et al., 2014; Walther et al., 2016). Yang et al. (2015) reported high diurnal and seasonal correlations between satellite-based and ground-based SIF as well as flux-tower based GPP in a deciduous forest.

Similar to photosynthesis, SIF is sensitive to water stress, and evidence of this has been demonstrated at different spatial scales (Flexas et al., 2002; Papageorgiou and Govindjee, 2014; Daumard et al., 2010; Porcar-Castell et al., 2014; Baker et al., 2008; Sun et al., 2015). At the leaf scale, for example, Flexas et al. [2002] reported a water stress-induced reduction of fluorescence yield under for C3 leaves. At the canopy scale, Daumard et al. [2010] found an SIF decrease during a drought episode, while canopy greenness was not affected. At the regional scale, Lee et al. [2013] found a simultaneous decrease of precipitation and SIF in the seasonally-dry Amazon rainforests. Sun et al. (2015) and Yoshida (2015) both found negative SIF responses to extreme drought events in the Great Plains of the U.S. and Russia. However, to the best of our knowledge, no efforts have been made to examine the response of SIF to seasonal water stress in the arid and semi-arid regions in Australia.

In this study, we used the SIF retrieved from the Global Ozone Monitoring Experiment-2 (GOME-2) (Joiner et al., 2013) and Orbiting Carbon Observatory-2 (OCO-

2) (Frankenberg et al., 2014) to examine vegetation seasonality in response to variations of water stress over the arid/semi-arid regions of Australia. The main goals of this study were (1) to evaluate the sensitivity of SIF to the seasonal variation of precipitation and (2) to compare the effectiveness and robustness of SIF, EVI, NDVI, and GPP in tracking the variation of plant activity and water availability in arid/semi-arid regions of Australia.

3.3. Data and Method

3.3.1. Precipitation dataset

Precipitation data were obtained from the Australia Bureau of Meteorology's network of rain gauges and weather stations (Jones et al., 2007, 2009). Twenty-four accumulated rainfalls from local time 9:00 A.M. one day to 9:00 A.M. the next day were measured at 3,000 sites across the country. Then, these rainfall values from about 3000 sites across the country were mapped onto 0.25 x 0.25-degree grids with quality control.

3.3.2. Satellite SIF dataset

At the canopy level, steady-state fluorescence from plant chlorophyll can be simply expressed as (e.g., Berry et al., 2013):

$$SIF = e * \varphi * fPAR * PAR, \quad (3.1)$$

where e is the fractional amount of fluorescence that escapes the canopy, theta is the fluorescence efficiency, and fPAR is the fraction of absorbed PAR. e* ϕ can be considered as the product of the actual fluorescence yield of the canopy and the fraction of the canopy emission that escapes to the atmosphere. In Equation (3.1), SIF, fPAR, and PAR can be estimated from remotely-sensed variables.

In this work, we used the SIF dataset from GOME-2 measurements for 2007 to 2015 (Joiner et al., 2013). GOME-2 is an operational, nadir-viewing, UV/visible, cross-

track scanning spectrometer. It is part of the European Meteorological Satellite (EUMETSAT) Polar System (EPS) MetOp mission series. GOME-2 measures the Earth's backscattered radiance and the extra-terrestrial solar irradiance at wavelengths between 240 and 790 nm in four detector channels. We used the retrieval of the far-red chlorophyll fluorescence peaking at 740 nm, which was estimated from measurements over a broad spectral range (734 - 758 nm) (Joiner et al., 2013, 2014). The resulting SIF data were gridded at 0.5° cell boxes and binned at monthly intervals. In addition, we applied SIF retrievals from the OCO-2 (Frankenberg et al., 2014) from January 2015 to December 2016. The OCO-2 mission was launched in July 2014, offering the possibility of monitoring SIF globally with a 100-fold improvement in spatial and temporal resolution with respect to other products, including GOME-2 and GOSAT (Frankenberg et al., 2014; Guanter et al., 2015).

3.3.3. Satellite EVI dataset

EVI is widely used as a proxy of canopy "greenness" to address spatial and temporal variations in terrestrial photosynthetic activity (e.g., Huete et al., 2002; Ma et al., 2013). EVI is expressed as (Huete et al., 1997):

$$EVI = G\frac{NIR - RED}{NIR + C_1 RED - C_2 BLUE + L}, \quad (3.2)$$

where L is the canopy background adjustment, and C_1, C_2 are the coefficients of the aerosol resistance term, G is the gain factor. Coefficients adopted for MODIS EVI algorithms are: $L = 1$, $C_1 = 6$, $C_2 = 7.5$, and $G = 2.5$ (Huete et al. 2002). NIR, RED, and $BLUE$ are atmospherically corrected, either fully or partially, values of surface near-infrared(841–876 nm), red(620–670 nm) and blue (459–479 nm) spectral reflectance. MODIS monthly VI products (MOD13A3.005) for February2000–2013 were obtained from the USGS repository (http://e4ftl01.cr.usgs.gov/MOLT/MOD13A3.005/). This

dataset is produced globally over land at 1-km resolution and monthly compositing periods from atmospherically corrected surface reflectance. The compositing algorithm is based on a constrained-view angle-maximum value composite (CV-MVC) to minimize atmospheric and bidirectional reflectance distribution function(BRDF) influences (Huete et al., 2002).

3.3.4. Satellite GPP dataset

The Gross Primary Production product (MOD17A2) is designed to provide an accurate regular measure of the growth of the terrestrial vegetation using daily MODIS landcover, fAPAR/LAI and surface meteorology at 1 km for the global vegetated land surface (Field et al., 1998). GPP values are calculated using MODIS greenness indices in conjunction with ancillary meteorological data as following:

$$GPP = \varepsilon_{max} * m(T_{min}) * m(VPD) * fPAR * SW_{rad} * 0.45, \quad (3.3)$$

where ε_{max} is the maximum land use efficiency (LUE) obtained from lookup tables on the basis of vegetation type. The scalars $m(T_{min})$ and $m(VPD)$ reduce ε_{max} under unfavorable conditions of low temperature and high VPD. $fPAR$ is the Fraction of Photosynthetically Active Radiation absorbed by the vegetation and SW_{rad} is shortwave solar radiation. T_{min}, VPD and SW_{rad} are obtained from large spatial-scale meteorological data sets that are available from the NASA Global Modeling and Assimilation Office (GMAO) (http://gmao.gsfc.nasa.gov/).

3.3.5. Methods

Figure 3.1 shows a map of the biomes on the continent of Australia, and the map includes tropical forests, temperate forests, croplands, and tropical savannahs and grasslands, as defined by Prentice et al. (YEAR). The analysis was done primarily over

"desert shrub and grassland" regions as marked in light brown with black outline. All of the datasets were remapped into 0.5 resolution from 2007 to 2015 except for OCO-2, which was available only from 2014 to 2016 with 2^{o} x 2^{o} resolution. Summary statistics of the average monthly values of SIF, NDVI, EVI, and precipitation were calculated over the entire study area. The leading and lagging cross correlations and the standard deviation of the monthly spatial averages were calculated to indicate the correlation of each variable with precipitation. In addition, the maximum and minimum values month map are shown in the spatial analysis.

3.4. RESULTS

Figure 3.1b shows that SIF followed the trend of precipitation throughout the year, reaching a maximum in January, decreasing continuously until September, and then starting to increase again near the end of the year. In contrast, EVI started at an intermediate value in January, increased to its maximum in April, decreased steadily to its lowest value in November, and started to increase again in December. The increase in EVI to its maximum value in April occurred in a period when precipitation decreased dramatically from the previous month. Therefore, SIF variations match the cycle of precipitation closely, i.e., highest in the summer season (December, January, and February) and lowest in the winter season (X, Y, and Z). The cycle of EVI is about three months behind the precipitation cycle. Figure 3.2c shows that the seasonal cycles of NIR and RED correlated with each other throughout the year. However, theoretically, they should change in opposite phases, i.e., when NIR reaches its maximum, RED should be at its minimum and vice versa. The mismatch suggests that the retrieval of red reflectance is confounded by the land background. Figure 3.1d shows the other variables, including NDVI and GPP, and it also shows similar, lagging cycles versus precipitation. The NDVI

curve forms a wave crest from March to July and a wave trough from October to December, lagging precipitation by about three months. MODIS GPP had two peaks, one in May and one in August, with its lowest points in November to January, which were almost exactly opposite phases from those of precipitation.

Figure 3.2 further supports the findings in Figs. 1b-d via spatial analyses. It represents the month when the maximum values occurred (left column) and minimum values (right column) for precipitation (PREC), SIF from different instruments (SIF_GOME2 and SIF_OCO-2), and EVI. It shows that the spatial pattern of SIF was more similar to that of precipitation (PREC) than EVI over the study area (desert area in Fig. 1a), especially for the month in which the maximum value occurred. Note that the month in which the minimum value of SIF (right column) occurred did not show a pattern similar to precipitation. That was because the vegetation was sparse in the arid and semi-arid regions. In the dry season (summer), the signal emitted by plants is very weak and hard to retrieve.

The lead and lag correlations show the extent of the correlation between a given variable and precipitation if the curve of the variable shifts earlier or later during certain months. For example, when the lag was three months, the correlation between precipitation and EVI was 0.9, which means that, if the EVI curve shifts to three months earlier, its correlation with the precipitation curve is 0.9. Since the lag of three months gave the largest positive correlation among all months, the change in EVI was considered to 'lag' precipitation by three months. Similarly, it can be concluded that the timing of SIF_GOMES2 matched precipitation perfectly, the timing of SIF_OCO-2 lagged slightly (for one month), and the timing of NIR lagged by five months.

3.5. CONCLUSIONS

The seasonal dynamics of vegetation were found to be sensitive to the availability of water throughout the region. Analysis of the lead-lag correlations between precipitation and SIF, EVI, and NDVI indicated that SIF and rainfall are well synchronized in their variations, but this was not the case for EVI and NDVI. Our results indicated that the retrieved fluorescence provides critical information about the seasonal dynamics associated with the production of vegetation.

We have demonstrated for the first time that SIF can be used to investigate the response of Australian arid/semiarid ecosystems to water stress on a seasonal scale. This is because SIF measures the light emissions that originate from the cores of the photosynthetic machinery, while other variables, such as EVI, NDVI, and MODIS GPP, cannot detect instantaneous and dynamic photosynthetic activity.

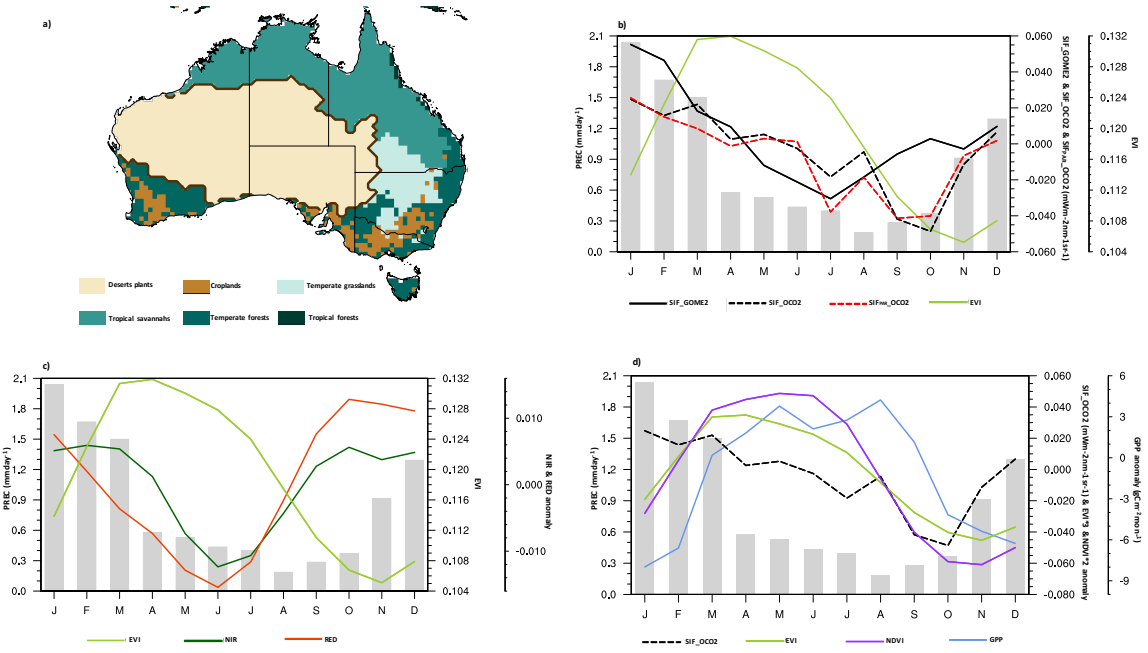

Figure 3.1. Vegetation map and time series of all biomass variables. a) is the vegetation type map of Australia continent. The study regions of arid/semiarid plants are shown in sand color with marked boarder. b)-d) are seasonal variation of different variables averaged over study region from 2007-2015 (for data retrieved from OCO-2 are from 2014-2016).

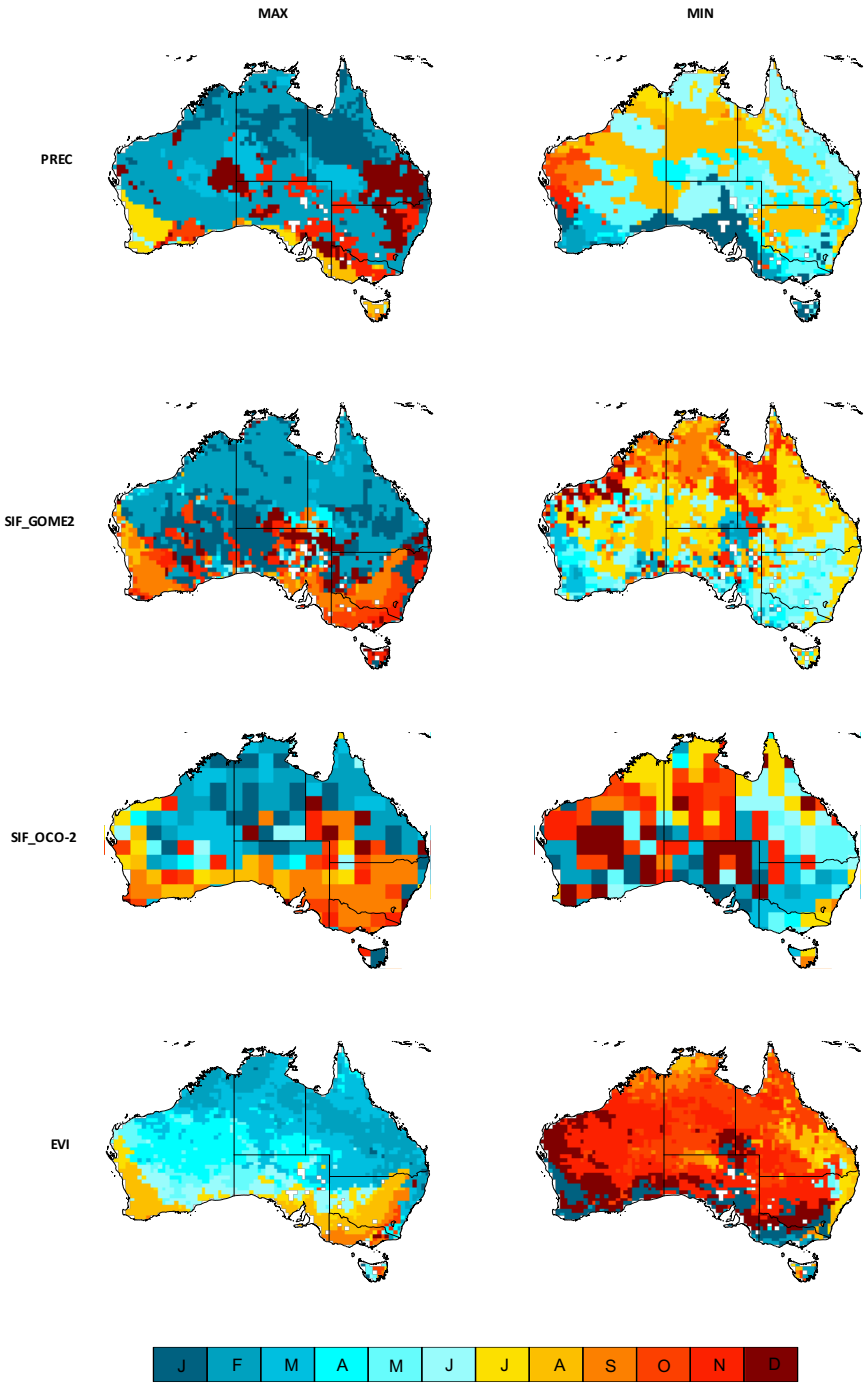

Figure 3.2. Spatial distribution of the month when maximum value or minimum value occurs.

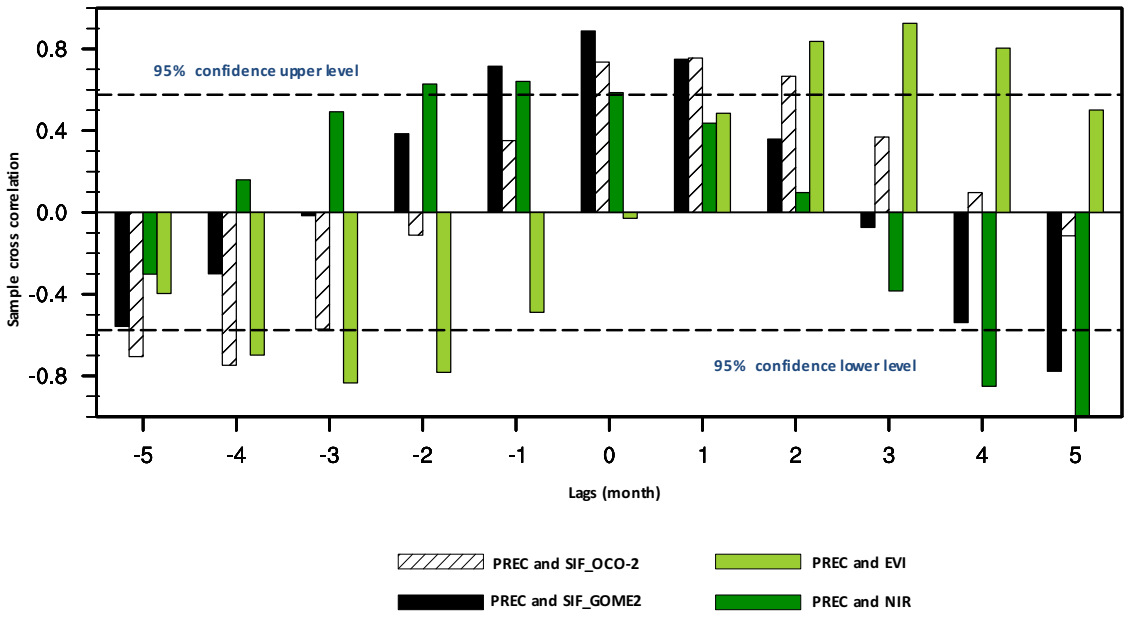

Figure 3.3. The correlation coefficients between precipitation(PREC) and the 5months lagging or leading plant related variables (SIF_OCO-2, SIF_GOME2, EVI, NIR).

CHAPTER 4: Disentangling climatic and anthropogenic controls on global terrestrial evapotranspiration trends

4.1. ABSTRACT

In this study, we examined the change of natural and anthropogenic controls on terrestrial evapotranspiration (ET) from 1982 to 2010 using multiple estimates from remote sensing-based datasets and process-oriented land surface models. A significant increasing trend of ET in each hemisphere was consistently revealed by observationally-constrained data and multi-model ensembles that considered historic natural and anthropogenic drivers. The climate impacts were simulated to determine the spatiotemporal variations in ET. Globally, rising CO_2 ranked second in these models after the predominant climatic influences, and yielded decreasing trends in canopy transpiration and ET, especially for tropical forests and high-latitude shrub land. Increasing nitrogen deposition slightly amplified global ET via enhanced plant growth. Land-use-induced ET responses, albeit with substantial uncertainties across the factorial analysis, were minor globally, but pronounced locally, particularly over regions with intensive land-cover changes. Our study highlights the importance of employing multi-stream ET and ET-component estimates to quantify the strengthening anthropogenic fingerprint in the global hydrologic cycle. Amazonia.

4.2. INTRODUCTION

An intensified global hydrological cycle has been observed and modeled during the past few years (Huntington 2006; Gerten et al., 2008; Wang et al., 2010; Durack et al., 2012; Douville et al., 2013; Sterling et al., 2013; Wu et al., 2013; Gedney et al., 2014). Terrestrial evapotranspiration (ET) is arguably the central component of this changing hydrologic cycle, and functions as a vital link between energy, water and

carbon cycles, thereby having important implications for the availability and usage of fresh water resources by humans and terrestrial ecosystems (Seneviratne et al., 2006; Trenberth et al., 2009; Fisher et al., 2011; Wang and Dickinson 2012).

Natural environmental factors (e.g. precipitation, temperature, incident solar radiation, soil moisture, wind and atmospheric teleconnections) regulate ET and its variability across different terrestrial ecosystems (Teuling et al., 2009; Jung et al., 2010; Wang et al., 2010; Vinukollu et al., 2011; Zhang et al., 2012; Miralles et al., 2014). These natural controls and limitations/co-limitations of ET are scale-dependent. Their mechanistic understanding is very important to predict the tendency and variability of ET (Wang and Dickinson, 2012). Human-induced land use/land cover change, ground water withdrawals, and irrigation can directly alter the amount and timing of ET by modifying the local water and energy balances (Piao et al., 2007; Gerten, 2013; Leung et al., 2013, 2014a, 2014b; Lo and Famiglietti, 2013; Sterling et al., 2013; Lei et al., 2014c). Human activities that contribute to greenhouse gas emissions, atmospheric nitrogen deposition (NDE), and ozone pollution can also alter ET indirectly through changes in physiological, structural and compositional responses of plants (Gedney et al., 2006; Betts et al., 2007; Sitch et al., 2007; Cao et al., 2009; Leakey et al., 2009). Discriminating these anthropogenic perturbations from natural factors is expected to increase in importance as anthropogenic transformation of the Earth System becomes more pervasive (Seneviratne et al., 2010; Gerten, 2013).

Based on mechanistic and empirical algorithms that are driven by remotely sensed observations, a variety of globally gridded diagnostic ET products have been compiled and evaluated in recent years (Willmott et al., 1985; Fisher et al., 2008; Jiménez et al., 2009; Jung et al., 2009; Sheffield et al., 2010; Zhang et al., 2010b; Miralles et al., 2011;

Mueller et al., 2011; Vinukollu et al., 2011; Zeng et al., 2012; Schwalm et al., 2013). These gridded ET estimates offer crucial sources and benchmarks for quantitative investigations of historical ET dynamics over the land surface. However, the accuracy of these observation-based ET products has yet to be reconciled due to limitations in underlying hypotheses and errors in input datasets (Mueller et al., 2011, 2013; Polhamus et al., 2012). Moreover, due to their reliance on the satellite observations, these datasets offer a limited historical temporal record that encompasses only a few decades (Badgley et al., 2015).

To predict future changes in ET patterns, process-based simulation and understanding of the magnitudes, mechanisms and interactions that control historical ET dynamics will be required and should be within uncertainty of both historical and present-day observations. Mechanistic land surface models (LSMs), driven by measurement-based environmental properties, are useful tools for the detection and attribution of natural and anthropogenic effects on ET dynamics. For the past decade, global factorial LSM experiments have been conducted and analyzed by different modeling groups to investigate the separate effects of environmental stresses on land surface and subsurface runoff, river flow, ET and water use efficiency (Gedney et al., 2006, 2014; Piao et al., 2007; Shi et al 2011, 2013; Tian et al., 2011; Liu et al., 2012; Tao et al., 2014). The role of climate impacts on these hydrologic variables has been characterized across different regions of the globe. The relative role of natural environmental change versus anthropogenic activities, however, was modeled to be heterogeneous and geographically dependent. Nevertheless, due to large differences in initial model conditions, driver data, and complex parameterizations that govern models,

the simulated ET was demonstrated to vary in magnitudes and responses across models at both temporal and spatial scales (Wang et al., 2010).

To disentangle these differences in simulated ET patterns and the relative role of model sensitivity and structure, the experimental setup and boundary/initial data must be similar among different participating models. We leveraged the controlled factorial experiments and model simulation protocol from the Multi-Scale Synthesis and Terrestrial Model Intercomparison Project (MsTMIP) (Huntzinger et al., 2013). Further, we synthesized a global ET time series (1982–2010) based on a diverse set of diagnostic ET products (Table 4.1), and the methodology reported recently in Mueller et al (2013). The partitioning of ET (e.g canopy transpiration (Tr) and evaporation from wet canopy and bare soil (ET–Tr)) and the variation of those ET components are poorly understood and less constrained by observations (Lawrence et al., 2007; Jasechko et al., 2013; Swenson and Lawrence, 2014; Wang et al., 2014). The MsTMIP modeling framework can advance our understanding of trends in ET by providing predictions of the individual ET components. In this study, we thus further investigated the contribution of individual influencing factors to the spatial and temporal characteristics of these ET constituents.

4.3. DATASETS AND METHODS

To We created a merged diagnostic ET data (DIA) from 11 long-term diagnostic datasets, all based on different assumptions and constrained with extensive in situ observations or satellite retrievals or both (Table 4.1). We remapped the monthly raw datasets from their original spatial resolutions to the half-degree resolution of the model output from 1982 through 2010 based on data availability. Following Mueller et al (2013), we applied both physical and statistical constraints for quality control and bias corrections. For the physical constraint, we developed a dataset of seasonal net radiation

maxima using the surface radiation budget (SRB3.0) datasets (Gupta, 1983). We then excluded grid points with values exceeding net radiation maxima by more than 25%. The outliers were identified as values that exceed ±3 standard deviations (Weedon, 2011). Then the median values of these quality-controlled multiple ET estimates were treated as the merged product, and were comprehensively compared with the LSM results in this study. As shown in Figure 4.5, the annual anomalies of the previously synthesized ET in Mueller et al (2013) are well within the spread of this newly-merged diagnostic data product. This updated product however, provides longer-term dynamics and is more amenable for studies at multi-decadal timescales.

To isolate the contributions of environmental drivers to multi-year ET variations, we utilized the factorial ET simulations from the MsTMIP data archive. Driven by the same environmental forcing (climate variability and trends, rising atmospheric CO2 concentrations causing fertilization and reducing stomatal opening, nitrogen deposition, land use/land cover change, and soil texture and vegetation types), these state-of-the-art LSMs were employed to identify the principal drivers of interannual variability and multi-decadal changes of ET. Because the evaporation component for canopy and soil, and the snow sublimation, were not separately archived in the standard model outputs in the MsTMIP I protocol (Huntzinger et al., 2013, 2015), we included all relevant available outputs, namely the ET, Tr and the total evaporation (ET–Tr). Four model experiments: (1) SG1 (time varying climate), (2) SG2 (time-varying climate and land use change history), (3) SG3 (time-varying climate, land use, and atmospheric CO2), and (4) BG1 (time-varying climate, land-use, atmospheric CO2 and nitrogen deposition), were analyzed to quantify the effects of each environmental forcing factor on the study variables for the years 1982 through 2010. The transient simulations began in 1901,

turning on one time-varying driver at a time. Simulations BG1 or SG3 were used to address the combined impacts from various historical forcing agents for models with (BG1) or without (SG3) an explicit nitrogen cycle. Simulation or simulation differencing was used to quantify the contribution to ET and ET component changes from climate change (CLI) (derived from SG1), land use/land cover change (LUC) (derived from SG2-SG1), rising atmospheric CO2 (CO2) (derived from SG3-SG2), NDE (derived from BG1-SG3), or all forcing (ALL) (derived from BG1 or SG3) (Table 4.1). To account for the overall effects from human activity (OTH), we derived the human-induced ET to be the difference between the BG1 and SG1 or SG3 and SG1 simulations.

Annual cropland area and total tree coverage information for the 1982–2010 period were derived from the merged product of the SYNergetic land cover MAP (Jung et al., 2006) and the annual time series of the land use harmonization data (Hurtt et al 2011). Additional details on the aforementioned driver data and experimental design can be found in Wei et al (2014a, 2014b) and Huntzinger et al (2013, 2015).

Growing season ET generally dominates the annual sum over the vegetated area of land (Wang et al., 2007). We focused our analysis on growing season ET for all observational and modeled data. The dynamic annual growing season information, used to mask the monthly ET between 1982 and 2010, was first determined from the global inventory modeling and mapping studies normalized difference vegetation index (NDVI3g) dataset (Pinzon and Tucker, 2014) using a Savitzky–Golay filter (Chen et al., 2004; Jonsson and Eklundh, 2004). It was then refined by excluding the freeze period identified by the Freeze/Thaw Earth System Data Record (Kim et al., 2011, 2012). In particular, the growing season of tropical rainforests was set to 12 months and it started in January.

4.4. RESULTS

Across the globe, statistically significant increasing trends of ET were recorded from 1982 to 2010 in the observation-based ET estimates (DIA) (1.18 mm yr^{-2}) and modeled ET from the ALL simulation (0.93 ± 0.31 mm yr^{-2}) (Figures 4.1 and 4.6, and Table 4.2). Significantly positive annual correlations between the simulated ALL ET and the observed ET were obtained, particularly in the Northern hemisphere (NH) (Land: $R^2 = 0.58, p < 0.01$, NH: $R^2 = 0.72, p < 0.01$, and the Southern hemisphere (SH): $R^2 = 0.46, p < 0.01$). The simulated multiyear increasing trend and interannual variability of the ALL ET were mainly explained by the CLI ET. In contrast, the overall human-induced OTH ET was predicted to decrease somewhat, and to exhibit relatively small interannual variations.

Spatial analysis of linear trends of ET for the merged observation product revealed remarkably consistent increasing tendency over most continents (Figure 4.2a). Local hotspots of reduced ET were diagnosed to occur in the arid regions of Western North America, central Africa, Northern China and Southeastern Asia. By contrast, the modeled changes of ALL ET underestimated the magnitude of ET changes in Eastern North America and Western Europe, and missed the ET decreases in central Africa. But the placement of increasing or decreasing trends in ALL ET largely agreed favorably with those of the observed ET trends, indicating the suitability of examining multi-year ET trends using the all-factor simulations.

Increasing nitrogen deposition led to increasing leaf area index (LAI) (Figures 4.4b and Figure 4.7b), and consequently to enhanced terrestrial ET, particularly over South America, Africa and Southeastern China (Figures 4.2(f) and 4.6). The areas undergoing strong increase in forest fraction and decrease in cropland fraction, such as in

central Eastern North America and central Europe, clearly showed increasing annual ET (Figures 4.2(g), 4.4(c) and (d)). In contrast, regions with evident loss of trees, such as Eastern China and Southeastern South America, show a downtrend of annual ET. Compared to the CO2 and nitrogen deposition effects, however, the effect of LUC on land ET was important locally. Relatively large uncertainties from the LUC were also found between individual models (Figures 4.6 and 4.10).

Trends for the Tr and total ET–Tr were dominated by the climatic changes across various continents. For Tr, 85.4% of the study area was impacted by the climatic changes, and 88.7% for ET–Tr (Figures 4.3(b), (c), 4.8(a)–(f)). Congruent with the response of ET changes to rising CO2 (48.4 ppm during the period 1982–2010), most areas, especially these regions covered by tropical broadleaf evergreen trees and high latitude shrubs, showed decreasing Tr. This is due to the CO2-induced reduction in stomatal conductance overwhelming the LAI-induced increase of canopy evaporation and transpiration under elevated CO2 concentration (Figures 4.3(e) and 4.8(j)). On the other hand, CO2 fertilization would enhance canopy LAI through increasing photosynthate allocation to leaves, and caused more canopy transpiration and evaporation than the reduced transpiration by CO2 physiological effects, especially over dry areas with sparse vegetation (e.g. the Western North America, central Eurasia, and Australia) (Figures 4.7(a) and 4.8(j)). Reversed ET–Tr trends in these arid regions imply that decreasing soil evaporation was the dominant factor in changing ET–Tr (Figures 4.8(j)–(l)). For most areas that showed decreasing Tr but increasing ET–Tr under CO2 enrichment, the augmented evaporation of intercepted rainfall and increasing soil evaporation may have been coincidental.

Increasing ET caused by nitrogen deposition was due to enhanced Tr (Figures 4.2(f), 4.8(m) and 4.9). A decrease of ET–Tr caused by the nitrogen deposition effect, as seen in central North America and in Western Europe, was due to reduced soil evaporation (Figures 4.8(n) and 4.9). The latter is a consequence of the increasing LAI providing more shade and so reducing solar energy for soil evaporation. In addition, the increasing Tr further depleted soil water, which reduced soil evaporation. In the evergreen broadleaf forests of the Western Amazon and Congo basin, nitrogen deposition and higher LAI resulted in increasing canopy evaporation. The increase in canopy evaporation more than offset the decrease in soil evaporation and hence dominated the increasing ET–Tr and even the nitrogen-induced increase in total ET (Figures 4.8(m)–(o)).

LUC led to a decreasing trend in Tr across densely inhabited regions that had experienced substantial land use perturbations (e.g. clearing trees for crops) during the study period. These occurred mainly in Southeastern South America and the Eastern China (Figures 4.4(c), (d), 4.8(p) and 4.9). Tr trends showed a general negative sign over central Eastern North America and Western Europe, where croplands had been replaced mainly by forests and woodlands. This reduction of Tr with reforestation implies that the tree species that replaced the crops had lower stomatal conductance than the crop species, the younger and smaller trees of the returning forests had lower LAI than the croplands they replaced, or the available soil water for plants decreased because of the removal of irrigation. These aspects deserve further study.

4.5. DISCUSSIONS

Between 1982 and 2010, the observation-based and simulated ALL ET consistently showed a significantly increasing trend across the globe. These findings are

consistent with previous studies, which reported an intensified global hydrological cycle in response to global warming following the Clausius–Clapeyron law (the relationship between equilibrium water vapor pressure and temperature, about 7% per °C of warming) (Held and Soden, 2006), as well as increasing importance of the radiative component of ET (Johnson and Sharma 2010). Climatic factors accounted for much of the spatial and temporal variations in terrestrial ET, Tr and ET–Tr. This supports previous studies regarding the prevalent climatic mechanisms controlling the long-term ET trends such as temperature, precipitation, soil moisture, energy and internal climate variability (Teuling et al., 2009; Jung et al., 2010; Wang et al., 2010; Vinukollu et al., 2011; Zhang et al., 2012; Ukkola and Prentice, 2013; Miralles et al., 2014).

In our study, the rising atmospheric CO2 concentration, as tested by model factorial experiments, induced an overall suppression of Tr and hence a general decreasing ET. Our results further suggest that the sign of change and regional pattern of these CO2 physiological effects on ET were moderated by changes in LAI. The overall response of ET was eventually determined by the balance among the changes of Tr, canopy evaporation and soil evaporation. These results are consistent with modeled and observed plant physiological responses to the increase of CO2 concentration in the atmosphere (Betts et al., 2007; Leakey et al., 2009). They also reiterate previous findings that show the concurrent physiological and structural responses of vegetation to rising CO2, and associated hydrological effects (Gedney et al., 2006; Leipprand and Gerten, 2006; Ainsworth and Rogers, 2007; Betts et al., 2007; Kurc and Small, 2007; Piao et al., 2007; Cao et al., 2009; Leakey et al., 2009; Lei et al., 2014b).

Simulation experiments that consider NDE showed enhanced global LAI as a result of increasing nutrient availability (Figures 4.4(b) and 4.7(b)). The nitrogen-induced

enhancement of canopy Tr and canopy evaporation, however, was regionally offset by decreasing soil evaporation, and led to lower ET for the nitrogen fertilization effect. Nonetheless, mineralized nitrogen in the rooting system was governed by not only the amount of deposited N, but also by leaching and denitrification, which are affected by environmental conditions (Hovenden et al., 2014). This highlights the necessity of better understanding the interactions among these environmental drivers, and the underlying mechanisms responsible for biogeochemical and hydrologic cycles.

Previous modeling studies (Boisier et al., 2012, 2014; Shi et al., 2013; Sterling et al., 2013; Tao et al., 2014) agree with our results that anthropogenic activities modified ET and its components locally, and human-induced LUC effects tended to counteract each other at a global scale. We found large uncertainties associated with LUC impacts among the MsTMIP LSMs, particularly over the NH and areas having marked land cover conversions. Though based on the same merged LUC dataset, different LSM groups prescribed the dynamic evolution of plant functional types with model-specific classifications (Wei et al., 2014a, 2014b). The sensitivity of biophysical and biogeochemical processes to the reconstructed historical scenario of LUC, moreover, varied considerably from model to model (Huntzinger et al 2013). For example, for the SIB3-JPL models, abnormally higher LUC ET was simulated over the NH and global land compared to that of other models (Figure 4.10). In SIB3-JPL, ET is a function of stomatal conductance and is sensitive to changes in photosynthetically active radiation (PAR). In LUC simulations, plant functional type changes over time, but the PAR is prescribed from present day NDVI climatology and is thus fixed to modern vegetation. This can lead to a bias in gross primary production in cases where grasslands are converted to forests, since the NDVI and resulting fraction of incident PAR absorbed by

green leaving in the canopy (fPAR) are calculated from a modern day forest ecosystem but used to estimate stomatal conductance and ET for the historical grassland it replaced. The sensitivity to land-use change and cultivated ecosystems (e.g., irrigated croplands) reinforce the need for better LUC characterization, improved parameterization of ET in croplands, and the development of forcing datasets (e.g., PAR) that are not artificially dependent upon land cover. Improvements in these areas may help reduce the large inter-model spreads in the responses of ET to LUC.

Quantitative estimation of ET partitioning has been refined recently, but information on long-term variations and the precise drivers of each ET component are lacking (Jasechko et al., 2013; Wang et al., 2014). By using a multi-model ensemble, we assessed the annual trends of the Tr and ET–Tr over nearly three decades, and further estimated their spatial-temporal responses to various environmental stresses. These modeled results, however, remain rather uncertain without observational constrains that are sufficiently long and representative. Comprehensive synthesis of long-term observation-constrained ET components is needed to improve our understanding of the controlling mechanisms, and to better characterize the partitioning schemes.

4.6. CONCLUSIONS

The relative contribution of climate and anthropogenic activities to the spatio-temporal changes in ET was quantitatively characterized with the newly-merged ET and multifactor ensemble simulations from MsTMIP. In the LSMs, climate, CO2, nitrogen deposition, and land use impacts were separated experimentally to determine the ET variations between 1982 and 2010. Climate, and in particular, changes in precipitation, was the dominant control of multi-year ET trends and variability. The overall CO2 physiological and structural effect induced decreasing plants transpiration and the total

ET, especially in areas where vegetation was dense. Compared to climate change and the elevated CO2 effects, the impacts of nitrogen deposition and land use change on ET were less important and acted locally. Other detailed explorations are needed, such as the implementation of more compelling statistical techniques and fully-coupled modeling systems (Douville et al 2013, Wu et al 2013, Gedney et al 2014) to detect and attribute the natural and anthropogenic effects on ET with more certainty. ET-related feedback studies are also required to account for land-atmosphere interactions and anthropogenic impacts in the integrated earth system models (Seneviratne et al 2010, Bond-Lamberty et al 2014, Collins et al 2015) and to understand future trajectories of drought (Sheffield et al 2012, Zarch et al 2015). Given that human activities continue to grow and intensify in the Anthropocene Epoch, we emphasize utilizing multi-stream datasets and multi-modeling frameworks to better diagnose and project anthropogenic influences on terrestrial ET, hydrologic cycle and overall climate change.

4.7. ACKNOWLEDGEMENT

This research was supported partially by the Terrestrial Ecosystem Science Scientific Focus Area (SFA), which is sponsored by the Terrestrial Ecosystem Science (TES) Program in the Climate and Environmental Sciences Division (CESD) of the Biological and Environmental Research Program in the US Department of Energy Office of Science.

Group	Name	Algorithm	Spatial Resolution	Precipitation Data	Time Period	Citation
Diagnostic ET	GLEAM	Modified Priestley-Taylor	0.25° x 0.25°	GPCP CMORPH	1982-2010	Miralles et al. (2011)
	CSIRO	Modified Penman-Monteith	0.5° x 0.5°	SILO	1984-2005	Zhang et al. (2010b)
	MPI	Empirically derived from FLUXNET	0.5° x 0.5°	GPCC	1982-2008	Jung et al. (2009)
	NTSG	Modified Penman-Monteith	0.5° x 0.5°	GPCC	1983-2006	Zhang et al. (2010a)
	PRUNI (3 sets of data)	Penman-Monteith/Priestley-Taylor (ISCCP, AVHRR, SRB)	0.25° x0.25°	Sheffield et al. (2006)	1984-2007	Sheffield et al. (2010)
	PT-JPL	Modified Priestley-Taylor	0.5° x 0.5°	Not required	1984-2006	Fisher et al. (2008)
	UDEL	Modified Thornthwaite water budget	0.5° x 0.5°	GHCN2	1980-2008	Willmott et al. (1985)
	PUB	Empirical method (TWSA, CRU)	0.5° x 0.5°	GRACE	1982-2009	Zeng et al. (2012)
	AWB	Water balance	0.5° x 0.5°	GPCP	1990-2006	Mueller et al. (2011a)

Group	Name	Algorithm	Spatial Resolution		Time Period	Citation	CLI	LUC	CO2	NDE	ALL	OTH
MsTMIP ET	CLM4	Modified Penman-Monteith	0.5° x 0.5°	CRUNCEP	1982-2010	Lawrence et al. (2007); Mao et al. (2012)	Y	Y	Y	Y	Y	Y
	DLEM	Penman-Monteith	0.5° x 0.5°	CRUNCEP	1982-2010	Tian et al. (2011, 2012)	Y	Y	Y	Y	Y	Y
	BIOME-BGC	Penman-Monteith	0.5° x 0.5°	CRUNCEP	1982-2010	Thornton et al. (2002)	Y	N	N	N	Y	Y
	CLASS-CTEM-N+	Modified Penman-Monteith	0.5° x 0.5°	CRUNCEP	1982-2010	Huang et al. (2011); Bartlett et al. (2006)	Y	Y	Y	Y	Y	Y
	CLM4-VIC	Modified Penman-Monteith	0.5° x 0.5°	CRUNCEP	1982-2010	Lei et al. (2014a)	Y	Y	Y	Y	Y	Y
	ISAM	Modified Penman-Monteith	0.5° x 0.5°	CRUNCEP	1982-2010	Jain et al. (1996)	Y	Y	Y	Y	Y	Y
	LPJ-WSL	Modified Penman-Monteith	0.5° x 0.5°	CRUNCEP	1982-2010	Sitch et al. (2003)	Y	Y	Y	N	Y	Y
	ORCHIDEE-LSCE	Modified Penman-Monteith	0.5° x 0.5°	CRUNCEP	1982-2010	Krinner et al. (2005)	Y	Y	Y	N	Y	Y
	SiB3-JPL	Penman-Monteith	0.5° x 0.5°	CRUNCEP	1982-2010	Baker et al. (2008)	Y	Y	Y	N	Y	Y
	SiBCASA	Penman-Monteith	0.5° x 0.5°	CRUNCEP	1982-2010	Schaefer et al. (2008, 2009)	Y	Y	Y	N	Y	Y
	TRIPLEX-GHG	Modified Penman-Monteith	0.5° x 0.5°	CRUNCEP	1982-2010	Peng et al. (2011)	N	N	Y	Y	Y	N
	VEGAS	Bulk Transfer Formula	0.5° x 0.5°	CRUNCEP	1982-2010	Zeng (2005)	Y	Y	Y	N	Y	Y
	VISIT	Penman-Monteith	0.5° x 0.5°	CRUNCEP	1982-2010	Ito and Inatomi (2012)	Y	Y	Y	N	Y	Y

Table 4.1. Overview of the diagnostic ET datasets used for the merged ET of this study,

and the simulated ET from MsTMIP models. Factorial results of the MsTMIP multi-model are ALL: the impact from all historical forcing factors, CLI: the impact from historical climate only, OTH: all anthropogenic impacts, CO2: the historical CO2 impact only, NDE: the historical nitrogen deposition impact only, LUC: the historical land use/land cover change impact only, Y: the availability of ET simulation for the particular impact, and N: the non-availability of ET simulation for the particular impact.

Regions	ET and ET apartments	DIA	ALL	CLI	OTH	CO2	NDE	LUC
	ET	**1.332**	**0.528**	**0.682**	0.003	**-0.065**	0.009	0.019
North America	T	--	**0.165**	**0.282**	**-0.113**	**-0.083**	**0.02**	-0.032
	ET-T	--	0.154	**0.248**	**0.04**	**-0.007**	**-0.007**	**0.047**
	ET	**2.056**	**1.297**	**1.372**	**-0.336**	**-0.289**	**0.062**	0.005
South America	T	--	**0.971**	**0.753**	**-0.266**	-0.286	**0.13**	**-0.157**
	ET-T	--	**1.364**	**1.966**	-0.016	**0.01**	**-0.003**	**-0.068**
	ET	**1.378**	**0.789**	**0.649**	0.01	**-0.057**	**0.014**	**0.066**
Europe	T	--	**0.317**	**0.483**	**-0.074**	**-0.074**	**0.033**	**-0.134**
	ET-T	--	**0.334**	**0.348**	**0.033**	**-0.014**	**-0.031**	-0.005
	ET	**1.326**	**1.911**	**2.003**	**-0.039**	**-0.083**	**0.074**	**-0.045**
Africa	T	--	**1.496**	**1.032**	0.018	**-0.05**	**0.124**	-0.037
	ET-T	--	**0.957**	**1.103**	-0.004	**-0.017**	**-0.022**	**-0.017**
	ET	**0.564**	**0.372**	**0.475**	-0.08	**-0.086**	**0.018**	-0.004
Asia	T	--	**0.253**	**0.206**	**-0.077**	**-0.078**	**0.032**	**-0.044**
	ET-T	--	0.305	**0.448**	**0.017**	**-0.016**	**-0.013**	**0.041**
	ET	0.861	**1.261**	1.2	**0.061**	-0.001	0.0004	**0.0052**
Australia	T	--	0.069	-0.011	0.013	**0.022**	**0.018**	-0.001
	ET-T	--	0.744	0.71	**-0.04**	**-0.029**	**-0.003**	**-0.053**
	ET	**1.182**	**0.858**	**0.926**	**-0.127**	**-0.101**	**0.043**	0.003
Global Land	T	--	**0.324**	**0.348**	**-0.067**	**-0.078**	**0.077**	**-0.099**
	ET-T	--	**0.553**	**0.604**	**0.043**	**-0.005**	**-0.009**	**-0.035**
	ET	**1.152**	**0.664**	**0.793**	**-0.144**	**-0.069**	**0.044**	-0.008
thern Hemisphere	T	--	**0.222**	**0.454**	**-0.058**	**-0.062**	**0.037**	**-0.068**
	ET-T	--	**0.418**	**0.444**	**0.025**	**-0.022**	**-0.013**	**-0.046**
	ET	**1.233**	**1.168**	**1.218**	**-0.155**	**-0.165**	**0.042**	-0.024
thern Hemisphere	T	--	0.268	**0.286**	**-0.097**	**-0.097**	**0.057**	**-0.17**
	ET-T	--	**0.889**	**0.644**	**0.09**	0.0003	-0.0004	-0.013

Table 4.2. Trend statistics in ET median values for the observation-based estimates (DIA)

and MsTMIP simulated results over different regions from 1982-2010. The DIA only has the ET trends, and MsTMIP simulations have the trends of ET, Tr and ET-Tr. The factorial results from the MsTMIP multi-model are ALL: the impact from all historical forcing factors, CLI: the impact from historical climate only, OTH: all the anthropogenic impact, CO2: the historical CO2 impact only, NDE: the historical nitrogen deposition impact only, LUC: the historical land use/land cover change impact only, Y: the availability of ET simulation for the particular impact, and N: the non-availability of ET simulation for the particular impact. Values in bold indicate statistically significant trend at the 90% level.

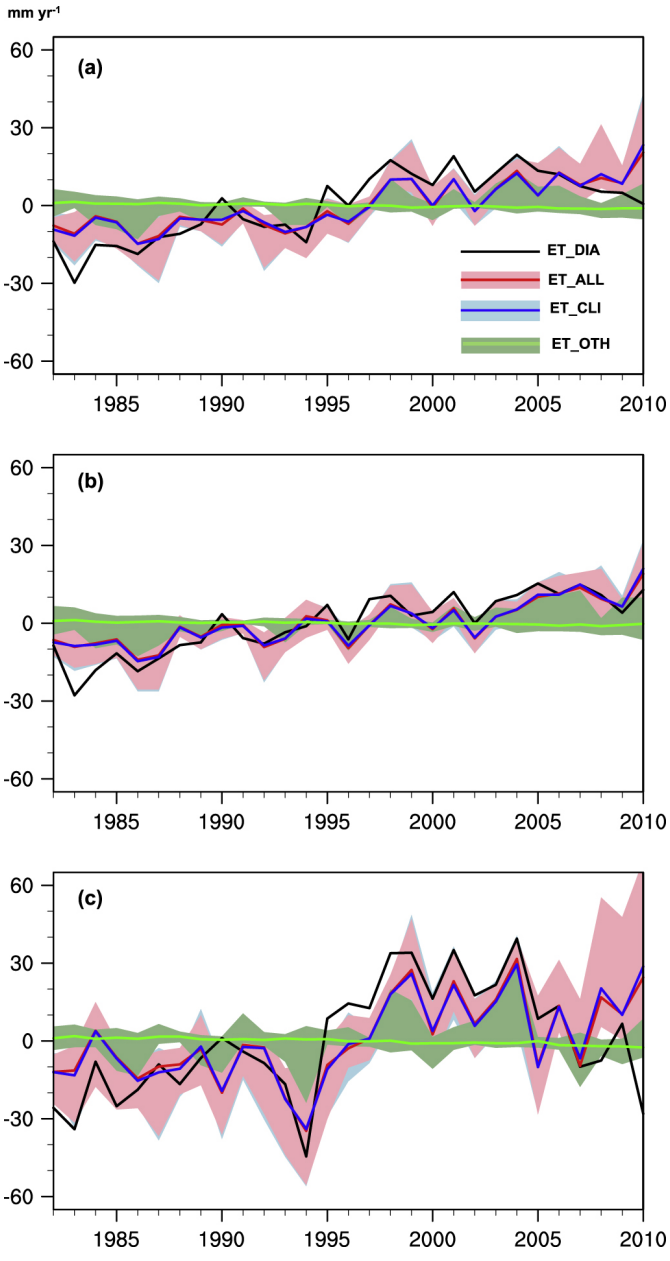

Figure 4.1. Time series of annual anomalies of growing season ET (mm yr^{-1}) over (a) the globe, (b) the NH, and (c) the SH from 1982 to 2010. Solid lines are the median values of the merged ET (ET_DIA, black), MsTMIP ET of ALL (ET_ALL, red), CLI (ET_CLI, blue), and OTH (ET_OTH, green). Shaded areas indicate the ET range of independent MsTMIP models.

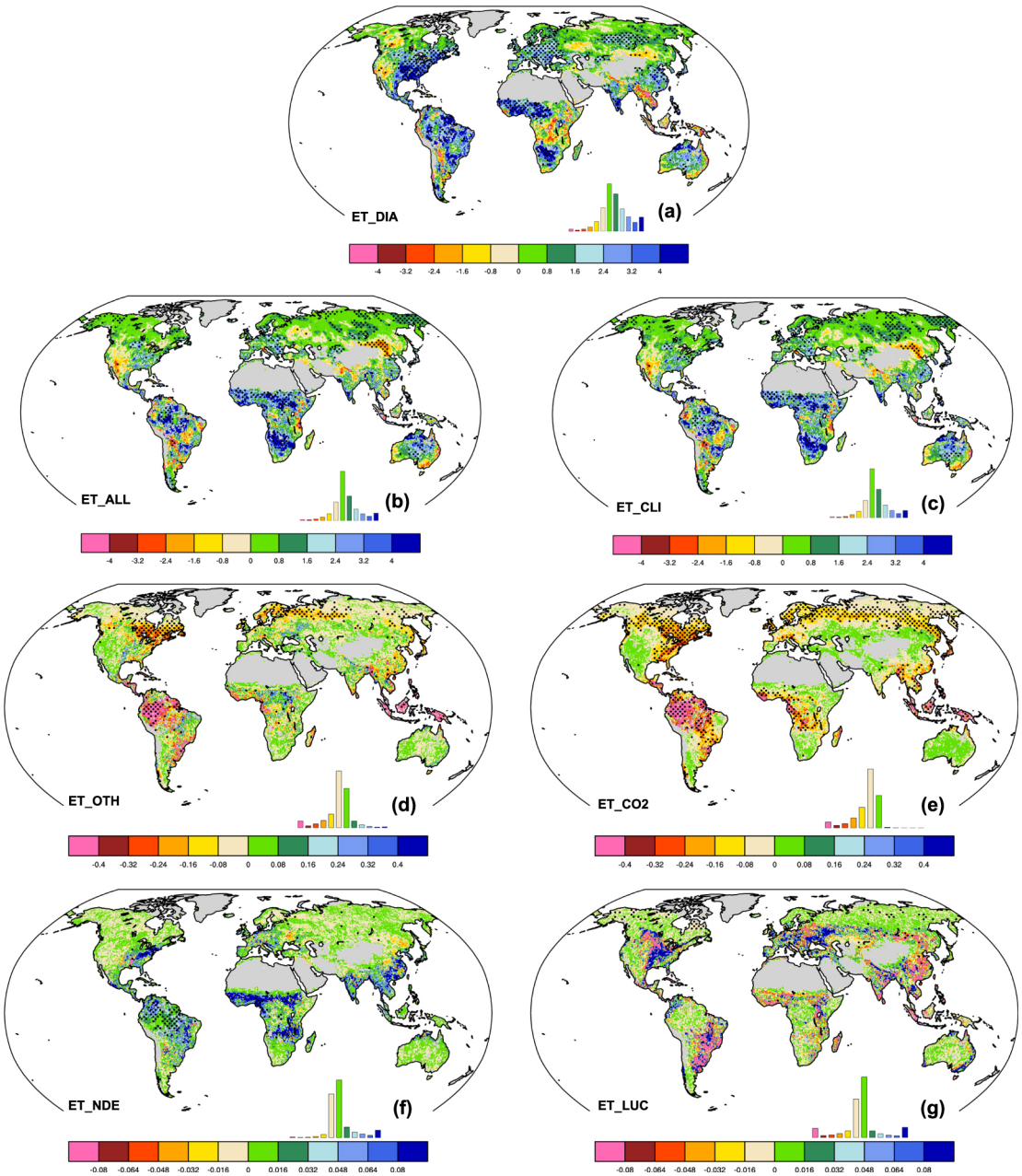

Figure 4.2. Spatial distribution of the linear trends in ET median values (mm yr^{-2}) for (a) ET_DIA, (b) ET_ALL, (c) ET_CLI, (d) ET_OTH, (e) CO2 (ET_CO2), (f) NDE (ET_NDE), and (g) LUC (ET_LUC) from 1982 to 2010. The stippled areas represent the trends are statistically significant ($P < 0.05$), and the insets show the frequency distribution of the corresponding change.

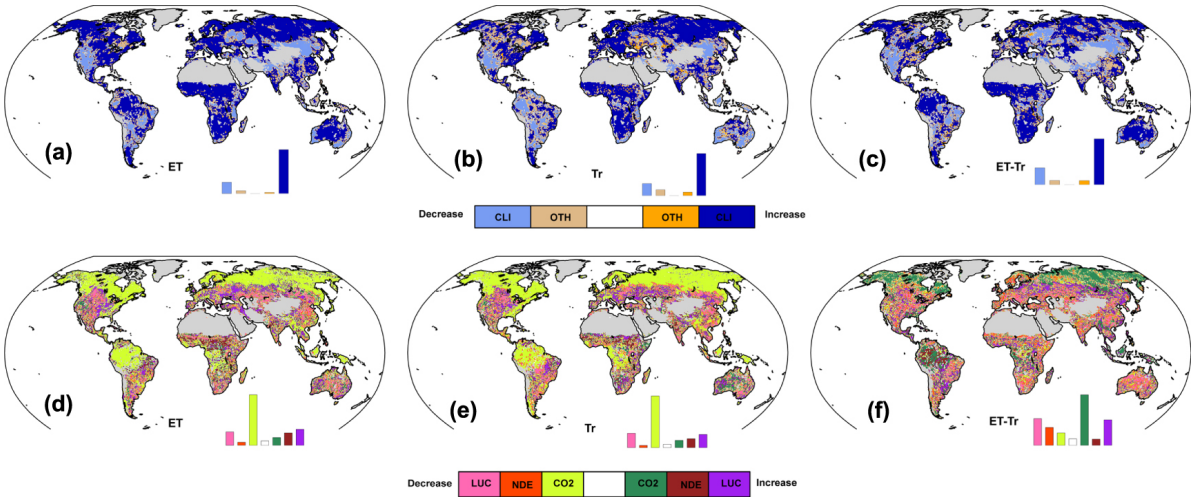

Figure 4.3. Spatial distribution of the dominant drivers for the ET, Tr and ET–Tr changes for the period 1982–2010. (a)–(c) Dominant drivers for the ET, Tr and ET–Tr trends of the ALL results, and (d)–(f) dominant drivers for the ET, Tr and ET–Tr trends of the OTH results.

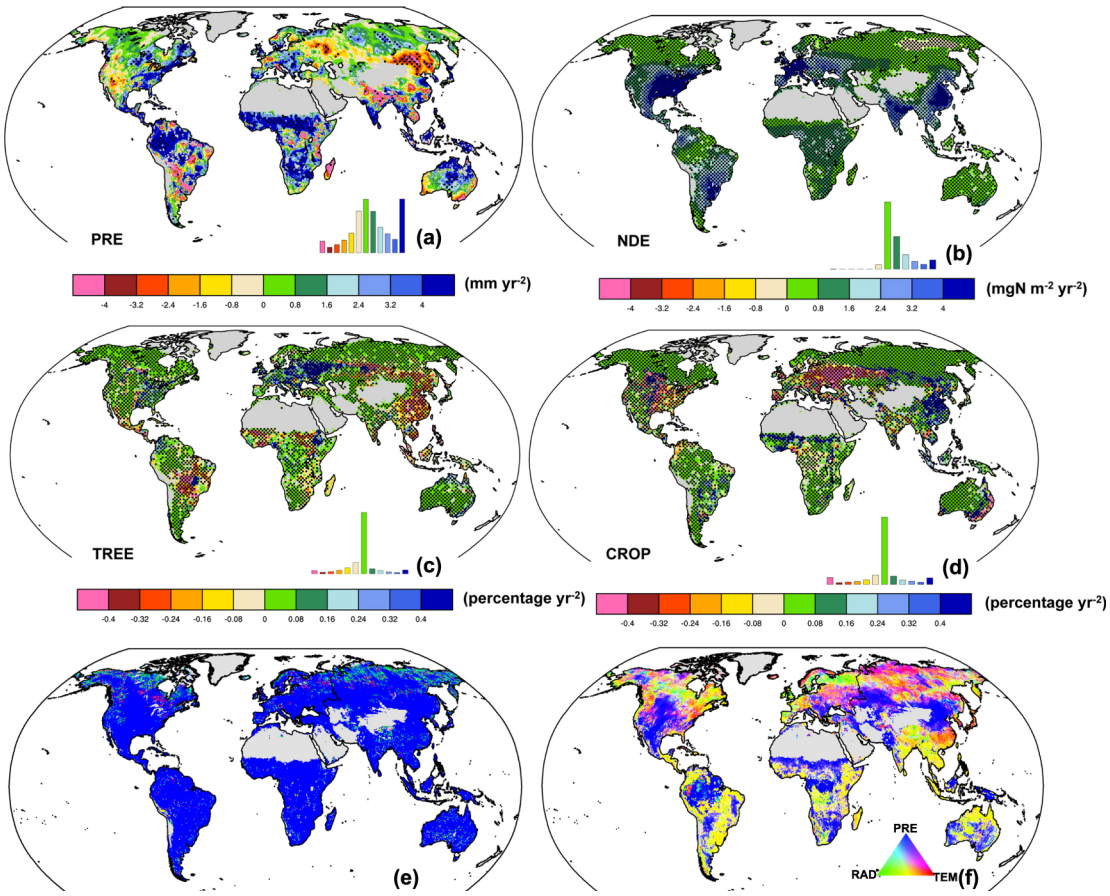

Figure 4.4. Spatial distribution of trends in (a) precipitation (PRE, mm yr^{-2}), (b) nitrogen deposition (NDE, mg N m^{-2} yr^{-2}), (c) fractional tree coverage (TREE, %/yr^2), and (d) fractional crop coverage (CROP, % yr^{-2}) over the period 1982–2010, and spatial distribution of dominant climatic variable (precipitation, temperature (TEM) and incident solar radiation (RAD)) responsible for (e) ET variability, and (f) both variability and trend. For (e), the dominance was derived by comparing the R2 of the partial correlations between detrended ET and individual climatic factor. For (f), the dominance was derived by comparing the R2 of the partial correlations between un-detrended ET and individual climatic factor. Both (e) and (f) share the same color legend in (f).

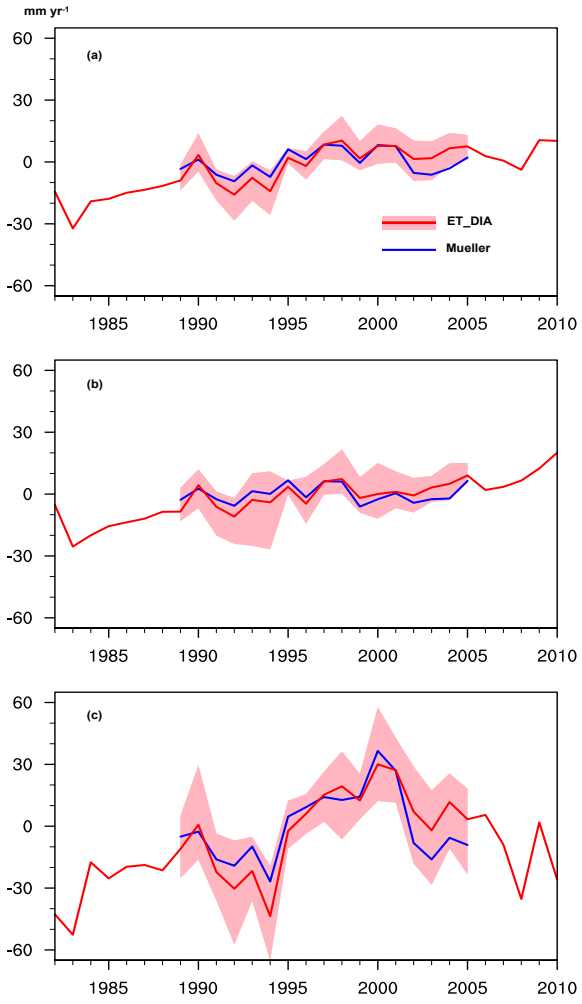

Figure 4.5. Time series of annual anomalies of ET (mm yr^{-1}) over (a) the globe, (b) the NH, and (c) the SH from 1982-2010. Solid lines are the median values of the merged ET from this study (ET_DIA, red), and the merged ET (Mueller, blue) from Mueller et al (2013). Shaded areas indicate the ±1 s.d. of ET_DIA for the overlapped period of the two datasets (1989-2005).

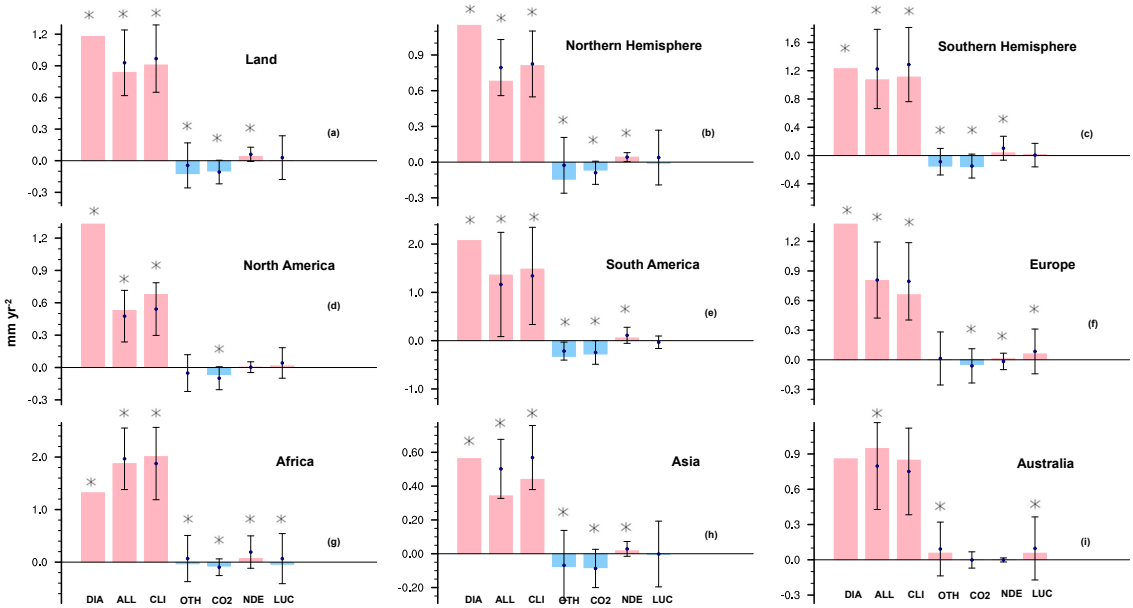

Figure 4.6. Trends of global-, NH-, SH- and continental-scale ET (mm yr^{-2}) for DIA, ALL, CLI, OTH, CO2, NDE and LUC results. *P < 0.05 for the trend in ET median values being significantly different from zero. For each category of the model results, the color bar represents the trend in ET median values of the individual model. The error bars indicate the mean±1 s.d. of ET trend for individual model within each category. The pink colors represent the positive trends and the blue colors denote the negative changes.

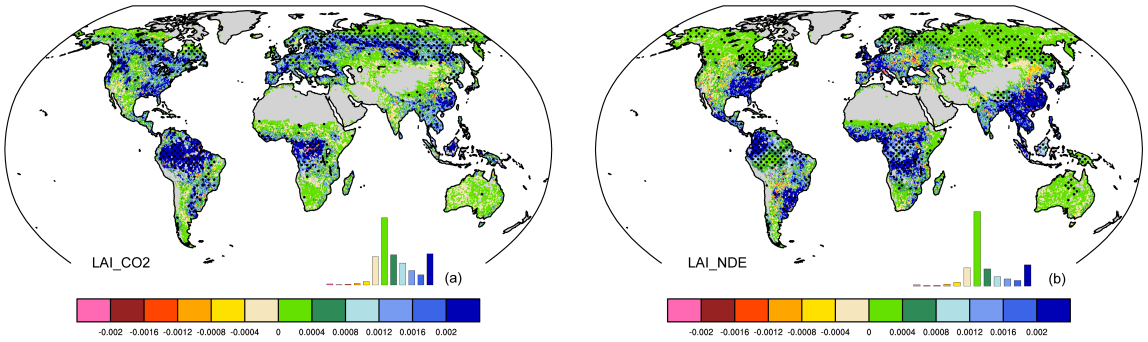

Figure 4.7. Spatial distribution of the linear trends in LAI (m^2 /m^2 /yr) for (a) CO2 result (LAI_CO2), and (b) NDE result (LAI_NDE) from 1982-2010.

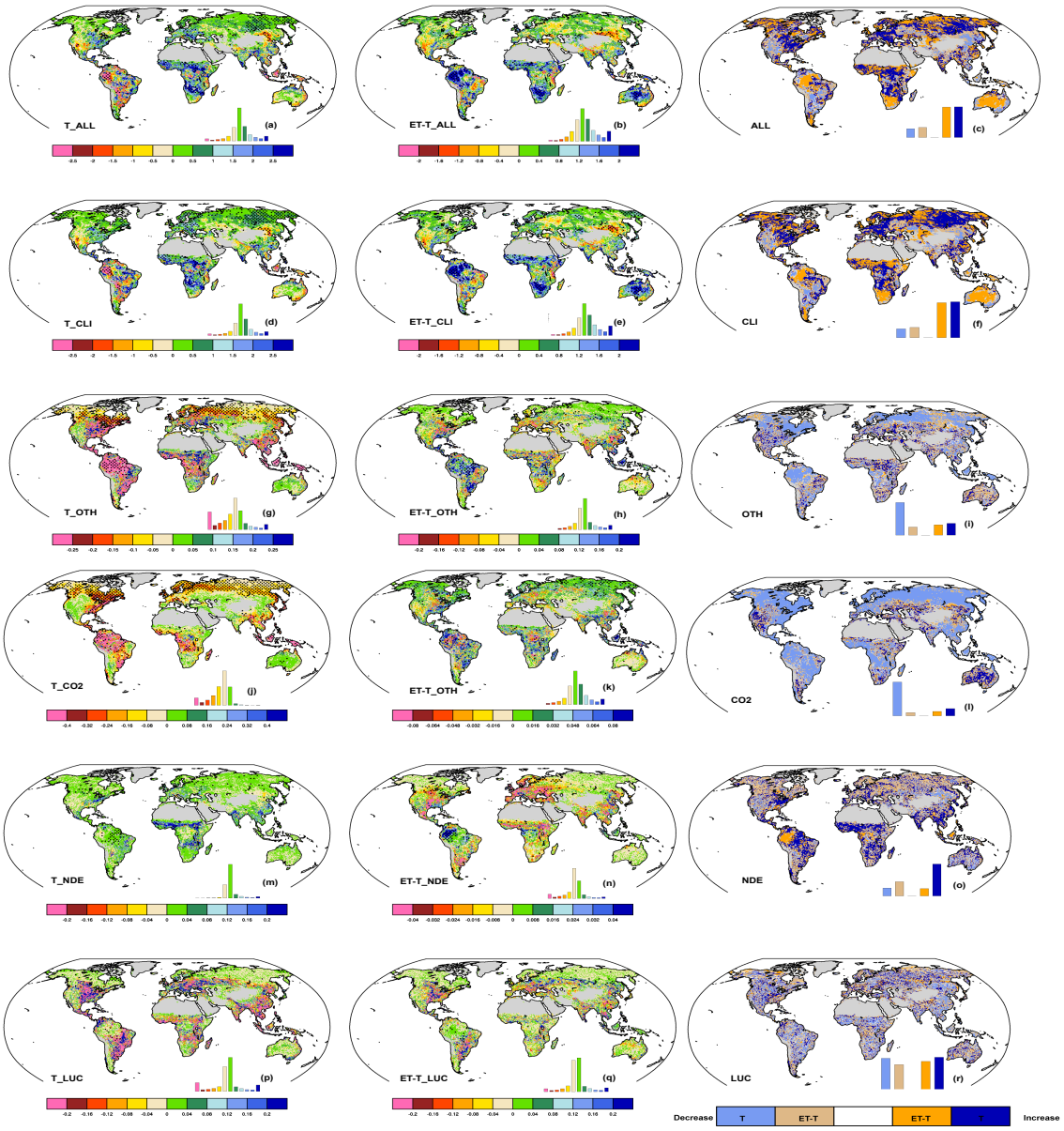

Figure 4.8. Spatial distribution of the linear trends in (a) ALL Tr (ALL_Tr), (b) ALL

ETTr (ET-Tr_ALL), (d) CLI Tr (CLI_Tr), (e) CLI ET-Tr (ET-Tr_CLI), (g) OTH Tr (OTH_Tr), (h) OTH ET-Tr (ET-Tr_OTH), (j) CO2 Tr (CO2_Tr), (k) CO2 ET-Tr (ETTr_ CO2), (m) NDE Tr (NDE_Tr), (n) NDE ET-Tr (ET-Tr_NDE), (p) LUC Tr (LUC_Tr), and (q) LUC ET-Tr (ET-Tr_LUC). The unit of Tr and ET-Tr trend is mm yr^{-2} . (c), (f), (i), (l), (o) and (r) show the spatial distribution of the dominant component (Tr or ET-Tr) for the ET changes of each category. The insets show the frequency distribution of the corresponding change.

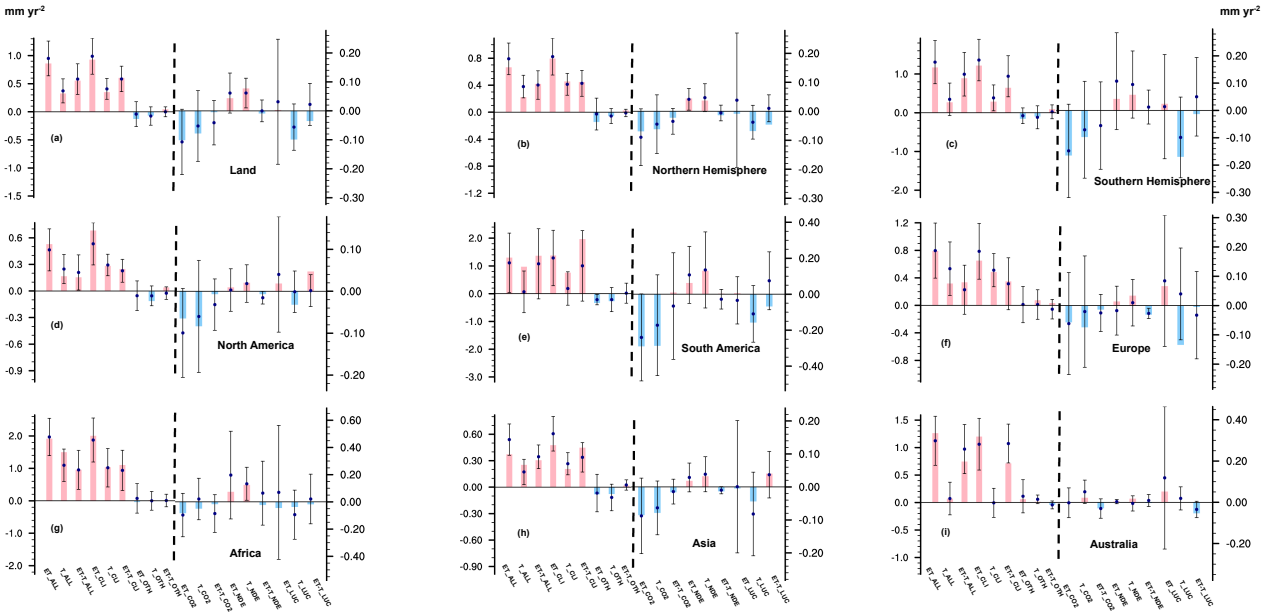

Figure 4.9. Trends of global-, NH-, SH- and continental-scale ET, Tr and ET-Tr (mm yr^{-2}). The results of ALL, CLI and OTH are associated with the left y axis, and those of CO2, NDE and LUC correspond to the right y axis. For each category of the model results, the color bar represents the trend in ET, Tr or ET-Tr median values of the individual model. The error bars indicate the mean±1 s.d. of ET, Tr or ET-Tr trend for individual model within each category. The pink colors represent the positive trends and the blue colors denote the negative changes.

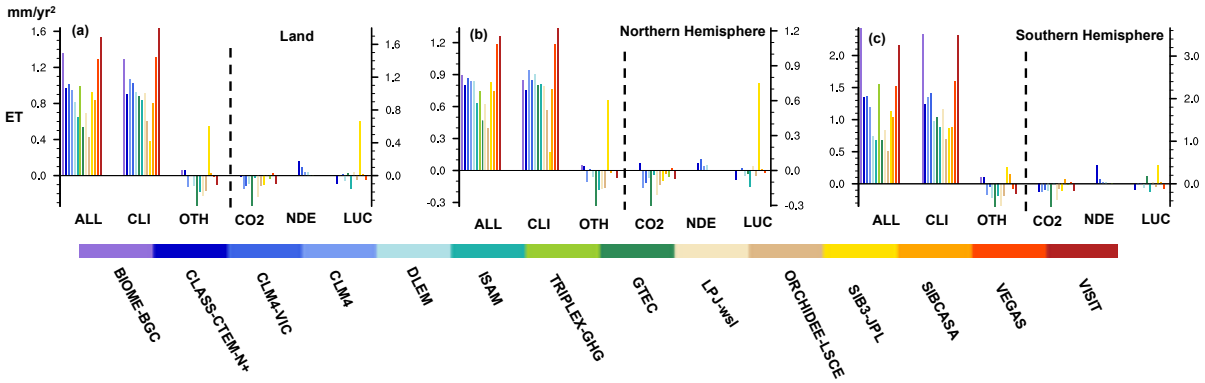

Figure 4.10. Trends of global-, NH- and SH- ET (mm yr^{-2}) for individual MsMTIP model. The results of ALL, CLI and OTH are associated with the left y axis, and those of CO2, NDE and LUC correspond to the right y axis.

CHAPTER 5: Summary and future work

5.1. SUMMARY

This dissertation focused on understanding the response of the biosphere to environmental conditions via modeling and analysis of observed data. The seasonal dry spell that lasts 1 to 6 months from northwest to southeast of the basin is the first type of water stress considered in this thesis. The first two main chapters (Chapters 2 and 3) are devoted to incorporating well-known, drought-coping mechanisms of trees into the Community Land Model (CLM), which is the land component of NCAR's Community Earth System Model (CESM). We evaluated the performance of the revised model by assessing whether the underestimation of dry-season water and energy fluxes can be corrected. Then, Chapter 4 focuses on how the El Niño events, which cause wide-spread, below-normal precipitation anomalies over large areas across the basin, especially the eastern portion, and influence the growth of vegetation on the inter-annual time scale. The seasonal difference of ENSO impact has also been studied.

Chapter 2 focuses on the response of isoprene emissions to environmental variables. We examined the separate effects of temperature and the water content of the soil on isoprene emissions at the MOFLUX site during two drought events, one in 2011 and one in 2012. We compared the observed data and the results of the MEGAN model simulation coupled with CLM 4.5 in different phases of the development of the drought. We found that temperature was a dominant factor under normal conditions without water stress. However, during a severe water deficit, exemplified by the peak stress phase, the impact of the moisture in the soil on isoprene emissions was more critical than the impact of temperature. Model simulations gave reasonably good predictions of isoprene emissions when compared to actual observations under non-stress conditions, but they

deviated from observations when the moisture in the soil was severely depleted. The discrepancies between the results of the models and observations during different drought phases suggest that the mechanisms by which moisture in the soil and temperature affect isoprene emissions during drought are not well represented in the isoprene emission model, which is overly sensitive to temperature variations. A more process-based, time-dependent algorithm is required to realistically interpret environmental impacts on isoprene emissions for different drought intensities and development phases.

In Chapter 3, the temporal dynamics of vegetation were found to be sensitive to the availability of water throughout the region with seasonal profiles. The analysis of the lead-lag correlation between precipitation and SIF, EVI, and NDVI indicated that SIF accounted for more of the variance in the rainfall. Our results suggested that retrieved fluorescence provides information that is independent of red reflectance and that it could be used to augment important information about the seasonal dynamics of global productivity. We demonstrated for the first time that SIF can be used to investigate the response of arid/semi-arid ecoregions to water stress on a seasonal scale. This is possible because SIF measures the light emissions that originate from the cores of the photosynthetic machinery, while other variables that are related indirectly to plant activity, such as the EVI, NDVI, and GPP, cannot detect actual instantaneous and dynamic photosynthetic activity.

The relative contributions of climate and anthropogenic activities to the spatio-temporal changes in ET were characterized quantitatively with the newly-merged ET and the multi-factor ensemble simulations from MsTMIP in Chapter 4. In the LSMs, climate, CO_2, nitrogen deposition, and land use impacts were separated experimentally to determine the variations in ET between 1982 and 2010. Climate was the dominant

determinant of the multi-year trends and variability of ET, and this was especially the case for precipitation. The overall physiological and structural effects of CO_2 induced decreasing transpiration in plants and decreased the total ET, especially in areas where vegetation was dense. Compared to climate change and the elevated effects of CO_2 effects, the impacts of nitrogen deposition and changes in land use on ET were less important and were mainly local. Other detailed explorations are needed, such as the implementation of more compelling statistical techniques and fully-coupled modeling systems to detect and attribute the natural and anthropogenic effects on ET with more certainty. ET-related feedback studies also are required to account for land-atmosphere interactions and anthropogenic impacts in the integrated Earth system models and to understand future trajectories of droughts. Given that human activities continue to increase and intensify in the Anthropocene Epoch, we emphasized the use of multi-stream datasets and multi-modeling frameworks to better diagnose and project anthropogenic influences on terrestrial ET, the hydrologic cycle, and overall climate change.

5.2. FUTURE WORK

The current modeling scheme for the emission of BVOCs emission is quite simplified, and many important aspects are not considered. Our analysis indicated that there is an urgent need for better models that can represent and predict the influence of moisture in the soil on isoprene emissions. An explicit soil-to-leaf mechanistic basis of drought-induced stress might be an optimal solution (Xu et al., 2016, New Phytologist; Sperry et al., 1998; Fisher et al., 2006, 2007). Also, increased isoprene emissions have been reported to improve the thermotolerance of leaves and to protect photosynthetic membranes from permanent damage during stressed conditions (Penuelas et al., 2005;

Sharkey and Singsaas, 1995; Velikova and Lereto, 2005; Sharkey et al., 2008), and this explains the continuing increase of isoprene emissions as temperature increases even after a drought has already started.

Potosnak et al. (2015) suggested that isoprene emissions should be decoupled from photosynthesis rather than sharing a similar water stress factor. Potosnak proposed a conceptual algorithm in which low moisture in the soil led to low photosynthesis, which increased the temperature of leaves. Isoprene emissions can continue for a period of time by using stored carbon, but, as the drought continues, the carbon reserves are depleted, and isoprene emissions decrease. In addition, Grote el al. (2016) and Dani et al. (2014) demonstrated mechanistic models that partition plant absorbed energy between photosynthesis and isoprenoid synthesis. The models can represent the effects of stomatal closure on isoprene emissions very well by coupling xxxx with the photosynthetic rate. Therefore, to better represent the effect of drought, the physiological variables of leaves and soil variables should be incorporated in the models in future work.

There are many land surface models, and there are even many different versions of the same model in some cases. For example, the CLM model we used to demonstrate the performance of the drought-coping mechanisms has been updated to the 4.5 version, and the 5.0 version is planned to be released in early 2017. Applying these modeling schemes to models of other land surfaces also is planned in the future.

In our study of SIF, we realize that it has great potential for detecting the actual activity of plants. In dryland areas with arid and semi-arid plants, we found that SIF can rapidly respond to the availability of water, which supports our initial premise. In future work, we will continue the seasonal scale study to quantify the beginnings and ends of seasons with SIF. The mid-to-high latitude forests will be our study area, because they

constitute a large carbon pool globally and are very sensitive to climate change. Also, current carbon models are inaccurate in the low temperature regime in the early Spring and in late Autumn. Thus, SIF holds great promise for identifying the phonological stage. It also can provide new insight into improving model simulations, because it appears to strongly constrain the parameters in simulations related to both leaf phenology and photosynthetic functioning.

References

Badgley, G. et al., 2015. On uncertainty in global terrestrial evapotranspiration estimates from choice of input forcing datasets. *Journal of Hydrometeorology*, 16(4), pp.1449–1455.

Baker, I.T. et al., 2008. Seasonal drought stress in the Amazon: Reconciling models and observations. *Journal of Geophysical Research: Biogeosciences*, 113(G1).

Bartlett, P.A., MacKay, M.D. & Verseghy, D.L., 2006. Modified snow algorithms in the Canadian land surface scheme: model runs and sensitivity analysis at three boreal forest stands. *Atmosphere-Ocean*, 44(3), pp.207–222.

Betts, R.A. et al., 2007. Projected increase in continental runoff due to plant responses to increasing carbon dioxide. *Nature*, 448(7157), pp.1037–1041.

Boisier, J.P. et al., 2012. Attributing the impacts of land-cover changes in temperate regions on surface temperature and heat fluxes to specific causes: results from the first LUCID set of simulations. *Journal of Geophysical Research: Atmospheres*, 117(D12).

Boisier, J.P., de Noblet-Ducoudré, N. & Ciais, P., 2014. Historical land-use-induced evapotranspiration changes estimated from present-day observations and reconstructed land-cover maps. *Hydrology and Earth System Sciences*, 18(9), pp.3571–3590.

Bond-Lamberty, B. et al., 2014. On linking an Earth system model to the equilibrium carbon representation of an economically optimizing land use model. *Geoscientific Model Development*, 7(6), p.2545.

Cao, L. et al., 2009. Climate response to physiological forcing of carbon dioxide simulated by the coupled Community Atmosphere Model (CAM3. 1) and Community Land Model (CLM3. 0). *Geophysical Research Letters*, 36(10).

Chen, J. et al., 2004. A simple method for reconstructing a high-quality NDVI time-series data set based on the Savitzky–Golay filter. *Remote sensing of Environment*, 91(3), pp.332–344.

Collins, W.D. et al., 2015. The integrated Earth System Model (iESM): formulation and functionality. *Geosci Model Dev Discuss*, 8(1), pp.381–427.

Douville, H. et al., 2013. Anthropogenic influence on multidecadal changes in reconstructed global evapotranspiration. *Nature Climate Change*, 3(1), pp.59–62.

Durack, P.J., Wijffels, S.E. & Matear, R.J., 2012. Ocean salinities reveal strong global water cycle intensification during 1950 to 2000. *science*, 336(6080), pp.455–458.

Fisher, J.B., Tu, K.P. & Baldocchi, D.D., 2008. Global estimates of the land–atmosphere water flux based on monthly AVHRR and ISLSCP-II data, validated at 16 FLUXNET sites. *Remote Sensing of Environment*, 112(3), pp.901–919.

Fisher, J.B., Whittaker, R.J. & Malhi, Y., 2011. ET come home: potential evapotranspiration in geographical ecology. *Global Ecology and Biogeography*, 20(1), pp.1–18.

Gedney, N. et al., 2006. Detection of a direct carbon dioxide effect in continental river runoff records. *Nature*, 439(7078), pp.835–838.

Gedney, N. et al., 2014. Detection of solar dimming and brightening effects on Northern Hemisphere river flow. *Nature Geoscience*, 7(11), pp.796–800.

Gerten, D., 2013. A vital link: water and vegetation in the Anthropocene. *Hydrology and Earth System Sciences*, 17(10), p.3841.

Gerten, D. et al., 2008. Causes of change in 20th century global river discharge. *Geophysical Research Letters*, 35(20).

Gupta, S.K., 1983. A radiative transfer model for surface radiation budget studies. *Journal of Quantitative Spectroscopy and Radiative Transfer*, 29(5), pp.419–427.

Held, I.M. & Soden, B.J., 2006. Robust responses of the hydrological cycle to global warming. *Journal of Climate*, 19(21), pp.5686–5699.

Hovenden, M.J., Newton, P.C.D. & Wills, K.E., 2014. Seasonal not annual rainfall determines grassland biomass response to carbon dioxide. *Nature*, 511(7511), pp.583–586.

Huang, S. et al., 2011. Analysis of nitrogen controls on carbon and water exchanges in a conifer forest using the CLASS-CTEM N+ model. *Ecological modelling*, 222(20), pp.3743–3760.

Huntington, T.G., 2006. Evidence for intensification of the global water cycle: review and synthesis. *Journal of Hydrology*, 319(1), pp.83–95.

Huntzinger, D.N. et al., 2013. The north american carbon program multi-scale synthesis and terrestrial model intercomparison project–part 1: Overview and experimental design. *Geoscientific Model Development*, 6(6), pp.2121–2133.

Huntzinger, D. et al., 2016. NACP MsTMIP: Global 0.5-deg Terrestrial Biosphere Model Outputs (version 1) in Standard Format. *ORNL DAAC, Oak Ridge, Tennessee, USA*.

Hurtt, G.C. et al., 2011. Harmonization of land-use scenarios for the period 1500–2100: 600 years of global gridded annual land-use transitions, wood harvest, and resulting secondary lands. *Climatic change*, 109(1–2), p.117.

Ito, A. & Inatomi, M., 2012. Use of a process-based model for assessing the methane budgets of global terrestrial ecosystems and evaluation of uncertainty. *Biogeosciences*, 9(2), pp.759–773.

Jain, A.K., Kheshgi, H.S. & Wuebbles, D.J., 1996. A globally aggregated reconstruction of cycles of carbon and its isotopes. *Tellus B*, 48(4), pp.583–600.

Jasechko, S. et al., 2013. Terrestrial water fluxes dominated by transpiration. *Nature*, 496(7445), pp.347–350.

Jimenez, C., Prigent, C. & Aires, F., 2009. Toward an estimation of global land surface heat fluxes from multisatellite observations. *Journal of Geophysical Research: Atmospheres*, 114(D6).

Jönsson, P. & Eklundh, L., 2004. TIMESAT—a program for analyzing time-series of satellite sensor data. *Computers & Geosciences*, 30(8), pp.833–845.

Johnson, F. & Sharma, A., 2010. A comparison of Australian open water body evaporation trends for current and future climates estimated from Class A evaporation pans and general circulation models. *Journal of Hydrometeorology*, 11(1), pp.105–121.

Jung, M. et al., 2006. Exploiting synergies of global land cover products for carbon cycle modeling. *Remote Sensing of Environment*, 101(4), pp.534–553.

Jung, M., Reichstein, M. & Bondeau, A., 2009. Towards global empirical upscaling of FLUXNET eddy covariance observations: validation of a model tree ensemble approach using a biosphere model. *Biogeosciences*, 6(10), pp.2001–2013.

Jung, M. et al., 2010. Recent decline in the global land evapotranspiration trend due to limited moisture supply. *Nature*, 467(7318), pp.951–954.

Kim, Y. et al., 2011. Developing a global data record of daily landscape freeze/thaw status using satellite passive microwave remote sensing. *IEEE Transactions on Geoscience and Remote Sensing*, 49(3), pp.949–960.

Kim, Y. et al., 2012. Satellite detection of increasing Northern Hemisphere non-frozen seasons from 1979 to 2008: Implications for regional vegetation growth. *Remote Sensing of Environment*, 121, pp.472–487.

Krinner, G. et al., 2005. A dynamic global vegetation model for studies of the coupled atmosphere-biosphere system. *Global Biogeochemical Cycles*, 19(1).

Kurc, S.A. & Small, E.E., 2007. Soil moisture variations and ecosystem-scale fluxes of water and carbon in semiarid grassland and shrubland. *Water Resources Research*, 43(6).

Lawrence, D.M. et al., 2007. The partitioning of evapotranspiration into transpiration, soil evaporation, and canopy evaporation in a GCM: impacts on land–atmosphere interaction. *Journal of Hydrometeorology*, 8(4), pp.862–880.

Leakey, A.D.B. et al., 2009. Elevated CO2 effects on plant carbon, nitrogen, and water relations: six important lessons from FACE. *Journal of experimental botany*, 60(10), pp.2859–2876.

Lei, H. et al., 2014. Sensitivity of global terrestrial gross primary production to hydrologic states simulated by the Community Land Model using two runoff parameterizations. *Journal of Advances in Modeling Earth Systems*, 6(3), pp.658–679.

Lei, H., Yang, D. & Huang, M., 2014. Impacts of climate change and vegetation dynamics on runoff in the mountainous region of the Haihe River basin in the past five decades. *Journal of Hydrology*, 511, pp.786–799.

Lei, H. et al., 2015. Simulated impacts of irrigation on evapotranspiration in a strongly exploited region: a case study of the Haihe River basin, China. *Hydrological Processes*, 29(12), pp.2704–2719.

Leipprand, A. & Gerten, D., 2006. Global effects of doubled atmospheric CO2 content on evapotranspiration, soil moisture and runoff under potential natural vegetation. *Hydrological Sciences Journal*, 51(1), pp.171–185.

Leng, G. et al., 2013. Modeling the effects of irrigation on land surface fluxes and states over the conterminous United States: Sensitivity to input data and model parameters. *Journal of Geophysical Research: Atmospheres*, 118(17), pp.9789–9803.

Leng, G. et al., 2014. Modeling the effects of groundwater-fed irrigation on terrestrial hydrology over the conterminous United States. *Journal of Hydrometeorology*, 15(3), pp.957–972.

Leng, G. et al., 2015. A comparative analysis of the impacts of climate change and irrigation on land surface and subsurface hydrology in the North China Plain. *Regional Environmental Change*, 15(2), pp.251–263.

Liu, M. et al., 2012. Effects of multiple environment stresses on evapotranspiration and runoff over eastern China. *Journal of Hydrology*, 426, pp.39–54.

Lo, M. & Famiglietti, J.S., 2013. Irrigation in California's Central Valley strengthens the southwestern US water cycle. *Geophysical Research Letters*, 40(2), pp.301–306.

Mao, J. et al., 2012. Remote sensing evaluation of CLM4 GPP for the period 2000–09. *Journal of Climate*, 25(15), pp.5327–5342.

Miralles, D.G. et al., 2011. Global land-surface evaporation estimated from satellite-based observations. *Hydrology and Earth System Sciences*, 15(2), p.453.

Miralles, D.G. et al., 2014. El Niño–La Niña cycle and recent trends in continental evaporation. *Nature Climate Change*, 4(2), pp.122–126.

Mueller, B. et al., 2011. Evaluation of global observations-based evapotranspiration datasets and IPCC AR4 simulations. *Geophysical Research Letters*, 38(6).

Mueller, B. et al., 2013. Benchmark products for land evapotranspiration: LandFlux-EVAL multi-data set synthesis. *Hydrology and Earth System Sciences*.

Peng, C. et al., 2011. A drought-induced pervasive increase in tree mortality across Canada's boreal forests. *Nature climate change*, 1(9), pp.467–471.

Piao, S. et al., 2007. Changes in climate and land use have a larger direct impact than rising CO2 on global river runoff trends. *Proceedings of the National academy of Sciences*, 104(39), pp.15242–15247.

Pinzon, J.E. & Tucker, C.J., 2014. A non-stationary 1981–2012 AVHRR NDVI3g time series. *Remote Sensing*, 6(8), pp.6929–6960.

Polhamus, A., Fisher, J.B. & Tu, K.P., 2013. What controls the error structure in evapotranspiration models? *Agricultural and forest meteorology*, 169, pp.12–24.

Schaefer, K. et al., 2008. Combined simple biosphere/Carnegie-Ames-Stanford approach terrestrial carbon cycle model. *Journal of Geophysical Research: Biogeosciences*, 113(G3).

Schaefer, K. et al., 2009. Improving simulated soil temperatures and soil freeze/thaw at high-latitude regions in the Simple Biosphere/Carnegie-Ames-Stanford Approach model. *Journal of Geophysical Research: Earth Surface*, 114(F2).

Schwalm, C.R. et al., 2013. Sensitivity of inferred climate model skill to evaluation decisions: a case study using CMIP5 evapotranspiration. *Environmental Research Letters*, 8(2), p.24028.

Seneviratne, S.I. et al., 2006. Land–atmosphere coupling and climate change in Europe. *Nature*, 443(7108), pp.205–209.

Seneviratne, S.I. et al., 2010. Investigating soil moisture–climate interactions in a changing climate: A review. *Earth-Science Reviews*, 99(3), pp.125–161.

Sheffield, J., Goteti, G. & Wood, E.F., 2006. Development of a 50-year high-resolution global dataset of meteorological forcings for land surface modeling. *Journal of Climate*, 19(13), pp.3088–3111.

Sheffield, J., Wood, E.F. & Munoz-Arriola, F., 2010. Long-term regional estimates of evapotranspiration for Mexico based on downscaled ISCCP data. *Journal of Hydrometeorology*, 11(2), pp.253–275.

Sheffield, J., Wood, E.F. & Roderick, M.L., 2012. Little change in global drought over the past 60 years. *Nature*, 491(7424), pp.435–438.

Shi, X. et al., 2011. The impact of climate, CO2, nitrogen deposition and land use change on simulated contemporary global river flow. *Geophysical Research Letters*, 38(8).

Shi, X. et al., 2013. Spatiotemporal patterns of evapotranspiration in response to multiple environmental factors simulated by the Community Land Model. *Environmental Research Letters*, 8(2), p.24012.

Sitch, S. et al., 2003. Evaluation of ecosystem dynamics, plant geography and terrestrial carbon cycling in the LPJ dynamic global vegetation model. *Global Change Biology*, 9(2), pp.161–185.

Sitch, S. et al., 2007. Indirect radiative forcing of climate change through ozone effects on the land-carbon sink. *Nature*, 448(7155), pp.791–794.

Sterling, S.M., Ducharne, A. & Polcher, J., 2013. The impact of global land-cover change on the terrestrial water cycle. *Nature Climate Change*, 3(4), pp.385–390.

Swenson, S.C. & Lawrence, D.M., 2014. Assessing a dry surface layer-based soil resistance parameterization for the Community Land Model using GRACE and FLUXNET-MTE data. *Journal of Geophysical Research: Atmospheres*, 119(17).

Tao, B. et al., 2014. Increasing Mississippi river discharge throughout the 21st century influenced by changes in climate, land use, and atmospheric CO2. *Geophysical Research Letters*, 41(14), pp.4978–4986.

Tian, H. et al., 2011. Net exchanges of CO2, CH4, and N2O between China's terrestrial ecosystems and the atmosphere and their contributions to global climate warming. *Journal of Geophysical Research: Biogeosciences*, 116(G2).

Tian, H. et al., 2012. Century-scale responses of ecosystem carbon storage and flux to multiple environmental changes in the southern United States. *Ecosystems*, 15(4), pp.674–694.

Teuling, A.J. et al., 2009. A regional perspective on trends in continental evaporation. *Geophysical Research Letters*, 36(2).

Thornton, P.E. et al., 2002. Modeling and measuring the effects of disturbance history and climate on carbon and water budgets in evergreen needleleaf forests. *Agricultural and forest meteorology*, 113(1), pp.185–222.

Trenberth, K.E., Fasullo, J.T. & Kiehl, J., 2009. Earth's global energy budget. *Bulletin of the American Meteorological Society*, 90(3), pp.311–323.

Ukkola, A.M. & Prentice, I.C., 2013. A worldwide analysis of trends in water-balance evapotranspiration. *Hydrology and Earth System Sciences*, 17(10), pp.4177–4187.

Vinukollu, R.K. et al., 2011. Multi-model, multi-sensor estimates of global evapotranspiration: climatology, uncertainties and trends. *Hydrological Processes*, 25(26), pp.3993–4010.

Wang, K. et al., 2007. A simple method to estimate actual evapotranspiration from a combination of net radiation, vegetation index, and temperature. *Journal of Geophysical Research: Atmospheres*, 112(D15).

Wang, K. et al., 2010. Evidence for decadal variation in global terrestrial evapotranspiration between 1982 and 2002: 1. Model development. *Journal of Geophysical Research: Atmospheres*, 115(D20).

Wang, K. & Dickinson, R.E., 2012. A review of global terrestrial evapotranspiration: Observation, modeling, climatology, and climatic variability. *Reviews of Geophysics*, 50(2).

Wang, L., Good, S.P. & Caylor, K.K., 2014. Global synthesis of vegetation control on evapotranspiration partitioning. *Geophysical Research Letters*, 41(19), pp.6753–6757.

Wei, Y. et al., 2014. The North American Carbon Program Multi-scale Synthesis and Terrestrial Model Intercomparison Project–Part 2: Environmental driver data, Geosci. Model Dev., 7, 2875–2893.

Willmott, C.J., Rowe, C.M. & Mintz, Y., 1985. Climatology of the terrestrial seasonal water cycle. *Journal of Climatology*, 5(6), pp.589–606.

Wu, P., Christidis, N. & Stott, P., 2013. Anthropogenic impact on Earth/'s hydrological cycle. *Nature Climate Change*, 3(9), pp.807–810.

Zarch, M.A.A., Sivakumar, B. & Sharma, A., 2015. Droughts in a warming climate: A global assessment of Standardized precipitation index (SPI) and Reconnaissance drought index (RDI). *Journal of Hydrology*, 526, pp.183–195.

Zeng, N., Mariotti, A. & Wetzel, P., 2005. Terrestrial mechanisms of interannual CO2 variability. *Global biogeochemical cycles*, 19(1).

Zeng, Z. et al., 2012. Global evapotranspiration over the past three decades: estimation based on the water balance equation combined with empirical models. *Environmental Research Letters*, 7(1), p.14026.

Zhang, K. et al., 2010. A continuous satellite-derived global record of land surface evapotranspiration from 1983 to 2006. *Water Resources Research*, 46(9).

Zhang, Y. et al., 2010. Using long-term water balances to parameterize surface conductances and calculate evaporation at 0.05 spatial resolution. *Water Resources Research*, 46(5).

Zhang, Y. et al., 2012. Decadal trends in evaporation from global energy and water balances. *Journal of Hydrometeorology*, 13(1), pp.379–391.

Ashworth, K., Wild, O. & Hewitt, C.N., 2010. Sensitivity of isoprene emissions estimated using MEGAN to the time resolution of input climate data. *Atmospheric Chemistry and Physics*, 10(3), pp.1193–1201.

Guenther, A. et al., 1995. A global model of natural volatile organic compound emissions. *Journal of Geophysical Research: Atmospheres*, 100(D5), pp.8873–8892.

Müller, J.-F. et al., 2008. Global isoprene emissions estimated using MEGAN, ECMWF analyses and a detailed canopy environment model. *Atmospheric Chemistry and Physics*, 8(5), pp.1329–1341.

Henrot, A.-J. et al., 2017. Implementation of the biogenic emission model MEGAN (v2. 1) into the ECHAM6-HAMMOZ chemistry climate model. *Geoscientific Model Development [= GMD]*.

Houweling, S., Dentener, F. & Lelieveld, J., 1998. The impact of nonmethane hydrocarbon compounds on tropospheric photochemistry. *Journal of Geophysical Research: Atmospheres*, 103(D9), pp.10673–10696.

Granier, C. et al., 2000. The impact of natural and anthropogenic hydrocarbons on the tropospheric budget of carbon monoxide. *Atmospheric Environment*, 34(29), pp.5255–5270.

Hu, W. et al., 2016. Volatility and lifetime against OH heterogeneous reaction of ambient isoprene-epoxydiols-derived secondary organic aerosol (IEPOX-SOA). *Atmospheric Chemistry and Physics*, 16(18), pp.11563–11580.

Collins, W.J. et al., 2002. The oxidation of organic compounds in the troposphere and their global warming potentials. *Climatic Change*, 52(4), pp.453–479.

Monson, R.K. et al., 2012. Modeling the isoprene emission rate from leaves. *New Phytologist*, 195(3), pp.541–559.

Tawfik, A.B. et al., 2012. Quantifying the contribution of environmental factors to isoprene flux interannual variability. *Atmospheric Environment*, 54, pp.216–224.

Monson, R.K. et al., 1994. Environmental and developmental controls over the seasonal pattern of isoprene emission from aspen leaves. *Oecologia*, 99(3), pp.260–270.

Arneth, A. et al., 2011. Global terrestrial isoprene emission models: sensitivity to variability in climate and vegetation. *Atmospheric Chemistry and Physics*, 11(15), pp.8037–8052.

Seco, R. et al., 2015. Ecosystem-scale volatile organic compound fluxes during an extreme drought in a broadleaf temperate forest of the Missouri Ozarks (central USA). *Global change biology*, 21(10), pp.3657–3674.

Geron, C., Harley, P. & Guenther, A., 2001. Isoprene emission capacity for US tree species. *Atmospheric Environment*, 35(19), pp.3341–3352.

Wiedinmyer, C. et al., 2005. Ozarks Isoprene Experiment (OZIE): Measurements and modeling of the "isoprene volcano." *Journal of Geophysical Research: Atmospheres*, 110(D18).

Guenther, A.B. et al., 2012. The Model of Emissions of Gases and Aerosols from Nature version 2.1 (MEGAN2. 1): an extended and updated framework for modeling biogenic emissions.

Kuhn, U. et al., 2004. Strong correlation between isoprene emission and gross photosynthetic capacity during leaf phenology of the tropical tree species Hymenaea courbaril with fundamental changes in volatile organic compounds emission composition during early leaf development. *Plant, Cell & Environment*, 27(12), pp.1469–1485.

Huang, L. et al., 2014. Annual variability in leaf area index and isoprene and monoterpene emissions during drought years in Texas. *Atmospheric Environment*, 92, pp.240–249.

Gulden, L.E., Yang, Z. & Niu, G., 2007. Interannual variation in biogenic emissions on a regional scale. *Journal of Geophysical Research: Atmospheres*, 112(D14).

Guenther, A., 1993. Isoprene and monoterpene emission rate variability: model evaluations and sensitivity analyses. *Journal of Geophysical Research*, 98.

Harley, P., 1996. Effects of light, temperature and canopy position on net photosynthesis and isoprene emission from sweetgum (Liquidambar styraciflua) leaves. *Tree Physiology*, 16.

Owen, S.M. et al., 2002. Light dependency of VOC emissions from selected Mediterranean plant species. *Atmospheric environment*, 36(19), pp.3147–3159.

Rodríguez-Calcerrada, J. et al., 2013. Leaf isoprene emission declines in Quercus pubescens seedlings experiencing drought–Any implication of soluble sugars and mitochondrial respiration? *Environmental and Experimental Botany*, 85, pp.36–42.

Sharkey, T.D. et al., 1996. Field measurements of isoprene emission from trees in response to temperature and light. *Tree Physiology*, 16(7), pp.649–654.

Rosenstiel, T.N. et al., 2003. Increased CO2 uncouples growth from isoprene emission in an agriforest ecosystem. *Nature*, 421(6920), pp.256–259.

Pegoraro, E. et al., 2004. Effect of elevated CO 2 concentration and vapour pressure deficit on isoprene emission from leaves of Populus deltoides during drought. *Functional Plant Biology*, 31(12), pp.1137–1147.

Wilkinson, M.J. et al., 2009. Leaf isoprene emission rate as a function of atmospheric CO2 concentration. *Global Change Biology*, 15(5), pp.1189–1200.

Fortunati, A. et al., 2008. Isoprene emission is not temperature-dependent during and after severe drought-stress: a physiological and biochemical analysis. *The Plant Journal*, 55(4), pp.687–697.

Funk, J.L., Mak, J.E. & Lerdau, M.T., 2004. Stress-induced changes in carbon sources for isoprene production in Populus deltoides. *Plant, Cell & Environment*, 27(6), pp.747–755.

Genard-Zielinski, A.-C. et al., 2014. Isoprene emissions from downy oak under water limitation during an entire growing season: what cost for growth? *PloS one*, 9(11), p.e112418.

Lathiere, J., Hewitt, C.N. & Beerling, D.J., 2010. Sensitivity of isoprene emissions from the terrestrial biosphere to 20th century changes in atmospheric CO2 concentration, climate, and land use. *Global Biogeochemical Cycles*, 24(1).

Pegoraro, E. et al., 2004. Effect of drought on isoprene emission rates from leaves of Quercus virginiana Mill. *Atmospheric Environment*, 38(36), pp.6149–6156.

Llusià, J. et al., 2008. Contrasting species-specific, compound-specific, seasonal, and interannual responses of foliar isoprenoid emissions to experimental drought in a Mediterranean shrubland. *International Journal of Plant Sciences*, 169(5), pp.637–645.

Lehning, A. et al., 1999. Isoprene synthase activity and its relation to isoprene emission in Quercus robur L. leaves. *Plant, Cell & Environment*, 22(5), pp.495–504.

Monson, R.K. et al., 1992. Relationships among isoprene emission rate, photosynthesis, and isoprene synthase activity as influenced by temperature. *Plant physiology*, 98(3), pp.1175–1180.

Rasulov, B. et al., 2010. Temperature response of isoprene emission in vivo reflects a combined effect of substrate limitations and isoprene synthase activity: a kinetic analysis. *Plant Physiology*, 154(3), pp.1558–1570.

Schnitzler, J.-P. et al., 2005. Biochemical properties of isoprene synthase in poplar (Populus× canescens). *Planta*, 222(5), pp.777–786.

Sun, Z. et al., 2013. Elevated [CO2] magnifies isoprene emissions under heat and improves thermal resistance in hybrid aspen. *Journal of experimental botany*, p.ert318.

Li, Z., Ratliff, E.A. & Sharkey, T.D., 2011. Effect of temperature on postillumination isoprene emission in oak and poplar. *Plant Physiology*, 155(2), pp.1037–1046.

Sanadze, G.A. & Kalandadze, A.N., 1966. Evolution of the diene C5H8 by poplar leaves under various conditions of illumination. *Doklady Akademii Nauk SSSR*, 168, pp.227–229.

Monson, R.K. et al., 2016. Interactions between temperature and intercellular CO2 concentration in controlling leaf isoprene emission rates. *Plant, Cell & Environment*, 39(11), pp.2404–2413.

Li, Z. & Sharkey, T.D., 2013. Molecular and pathway controls on biogenic volatile organic compound emissions. In *Biology, controls and models of tree volatile organic compound emissions*. Springer, pp. 119–151.

Potosnak, M.J., LeStourgeon, L. & Nunez, O., 2014. Increasing leaf temperature reduces the suppression of isoprene emission by elevated CO 2 concentration. *Science of the Total Environment*, 481, pp.352–359.

Peñuelas, J. & Staudt, M., 2010. BVOCs and global change. *Trends in plant science*, 15(3), pp.133–144.

Wolfertz, M. et al., 2004. Rapid regulation of the methylerythritol 4-phosphate pathway during isoprene synthesis. *Plant Physiology*, 135(4), pp.1939–1945.

Rasulov, B. et al., 2009. Postillumination isoprene emission: in vivo measurements of dimethylallyldiphosphate pool size and isoprene synthase kinetics in aspen leaves. *Plant Physiology*, 149(3), pp.1609–1618.

Huang, L. et al., 2015. Quantifying regional, seasonal and interannual contributions of environmental factors on isoprene and monoterpene emissions estimates over eastern Texas. *Atmospheric Environment*, 106, pp.120–128.

Wiedinmyer, C. et al., 2001. A land use database and examples of biogenic isoprene emission estimates for the state of Texas, USA. *Atmospheric Environment*, 35(36), pp.6465–6477.

Stavrakou, T. et al., 2014. Isoprene emissions over Asia 1979–2012: impact of climate and land-use changes. *Atmospheric Chemistry and Physics*, 14(9), pp.4587–4605.

Gu, L. et al., 2006. Direct and indirect effects of atmospheric conditions and soil moisture on surface energy partitioning revealed by a prolonged drought at a temperate forest site. *Journal of Geophysical Research: Atmospheres*, 111(D16).

Gu, L. et al., 2007. Influences of biomass heat and biochemical energy storages on the land surface fluxes and radiative temperature. *Journal of Geophysical Research: Atmospheres*, 112(D2).

Gu, L. et al., 2015. Drought-influenced mortality of tree species with different predawn leaf water dynamics in a decade-long study of a central US forest.

Potosnak, M.J. et al., 2014. Observed and modeled ecosystem isoprene fluxes from an oak-dominated temperate forest and the influence of drought stress. *Atmospheric environment*, 84, pp.314–322.

Young, F.J., Radatz, C.A. & Marshall, C.A., 2003. Soil survey of Boone County, Missouri.

Garrett, H.E. & Cox, G.S., 1973. Carbon dioxide evolution from the floor of an oak-hickory forest. *Soil Science Society of America Journal*, 37(4), pp.641–644.

Karl, T. et al., 2001. Eddy covariance measurement of biogenic oxygenated VOC emissions from hay harvesting. *Atmospheric Environment*, 35(3), pp.491–495.

Pallardy, S.G., Pereira, J.S. & Parker, W.C., 1991. Measuring the state of water in tree systems. *Techniques and approaches in forest tree ecophysiology. CRC Press, Boca Raton, Fla*, pp.28–76.

Turner, N.C., 1981. Correction of flow resistances of plants measured from covered and exposed leaves. *Plant Physiology*, 68(5), pp.1090–1092.

Yang, B.A.I. et al., 2010. Environmental controls on water use efficiency during severe drought in an Ozark Forest in Missouri, USA. *Global Change Biology*, 16(8), pp.2252–2271.

Belden, A.C. & Pallardy, S.G., 2009. Successional trends and apparent Acer saccharum regeneration failure in an oak-hickory forest in central Missouri, USA. *Plant Ecology*, 204(2), pp.305–322.

Oleson, K.W. et al., 2010. Technical description of version 4.0 of the Community Land Model (CLM).

Xue, Y. et al., 1991. A simplified biosphere model for global climate studies. *Journal of Climate*, 4(3), pp.345–364.

Du, E., Di Vittorio, A. & Collins, W.D., 2016. Evaluation of hydrologic components of community land model 4 and bias identification. *International Journal of Applied Earth Observation and Geoinformation*, 48, pp.5–16.

Xu, X. et al., 2016. Diversity in plant hydraulic traits explains seasonal and inter-annual variations of vegetation dynamics in seasonally dry tropical forests. *New Phytologist*, 212(1), pp.80–95.

Fisher, R.A. et al., 2007. The response of an Eastern Amazonian rain forest to drought stress: results and modelling analyses from a throughfall exclusion experiment. *Global Change Biology*, 13(11), pp.2361–2378.

Fisher, R.A. et al., 2006. Evidence from Amazonian forests is consistent with isohydric control of leaf water potential. *Plant, Cell & Environment*, 29(2), pp.151–165.

Sperry, J.S. et al., 1998. Limitation of plant water use by rhizosphere and xylem conductance: results from a model. *Plant, Cell & Environment*, 21(4), pp.347–359.

Dani, K.G.S. et al., 2014. Increased ratio of electron transport to net assimilation rate supports elevated isoprenoid emission rate in eucalypts under drought. *Plant Physiology*, 166(2), pp.1059–1072.

Arab, L. et al., 2016. Acclimation to heat and drought—Lessons to learn from the date palm (Phoenix dactylifera). *Environmental and Experimental Botany*, 125, pp.20–30.

Yuan, X. et al., 2016. Interaction of drought and ozone exposure on isoprene emission from extensively cultivated poplar. *Plant, Cell & Environment*, 39(10), pp.2276–2287.

Grote, R. et al., 2014. A fully integrated isoprenoid emissions model coupling emissions to photosynthetic characteristics. *Plant, cell & environment*, 37(8), pp.1965–1980.

Crisp, D., Miller, C.E. & DeCola, P.L., 2008. NASA Orbiting Carbon Observatory: measuring the column averaged carbon dioxide mole fraction from space. *Journal of Applied Remote Sensing*, 2(1), p.23508.

Lee, J.-E. et al., 2013. Forest productivity and water stress in Amazonia: observations from GOSAT chlorophyll fluorescence. *Proceedings of the Royal Society of London B: Biological Sciences*, 280(1761), p.20130171.

Huete, A.R. et al., 1997. A comparison of vegetation indices over a global set of TM images for EOS-MODIS. *Remote sensing of environment*, 59(3), pp.440–451.

Anav, A. et al., 2015. Spatiotemporal patterns of terrestrial gross primary production: A review. *Reviews of Geophysics*, 53(3), pp.785–818.

Baker, N.R., 2008. Chlorophyll fluorescence: a probe of photosynthesis in vivo. *Annu. Rev. Plant Biol.*, 59, pp.89–113.

Bastos, A. et al., 2013. The global NPP dependence on ENSO: La Niña and the extraordinary year of 2011. *Journal of Geophysical Research: Biogeosciences*, 118(3), pp.1247–1255.

Daumard, F. et al., 2010. A field platform for continuous measurement of canopy fluorescence. *IEEE Transactions on Geoscience and Remote Sensing*, 48(9), pp.3358–3368.

Sun, Y. et al., 2015. Drought onset mechanisms revealed by satellite solar-induced chlorophyll fluorescence: Insights from two contrasting extreme events. *Journal of Geophysical Research: Biogeosciences*, 120(11), pp.2427–2440.

Field, C.B., Randerson, J.T. & Malmström, C.M., 1995. Global net primary production: combining ecology and remote sensing. *Remote sensing of Environment*, 51(1), pp.74–88.

Zhang, Y. et al., 2014. Estimation of vegetation photosynthetic capacity from space-based measurements of chlorophyll fluorescence for terrestrial biosphere models. *Global change biology*, 20(12), pp.3727–3742.

Frankenberg, C. et al., 2014. Prospects for chlorophyll fluorescence remote sensing from the Orbiting Carbon Observatory-2. *Remote Sensing of Environment*, 147, pp.1–12.

Frankenberg, C. et al., 2011. New global observations of the terrestrial carbon cycle from GOSAT: Patterns of plant fluorescence with gross primary productivity. *Geophysical Research Letters*, 38(17).

Joiner, J. et al., 2013. Global monitoring of terrestrial chlorophyll fluorescence from moderate spectral resolution near-infrared satellite measurements: Methodology, simulations, and application to GOME-2. *Atmospheric Measurement Techniques*, 6(2), pp.2803–2823.

Jung, M. et al., 2011. Global patterns of land-atmosphere fluxes of carbon dioxide, latent heat, and sensible heat derived from eddy covariance, satellite, and meteorological observations. *Journal of Geophysical Research: Biogeosciences*, 116(G3).

Köhler, P., Guanter, L. & Joiner, J., 2015. A linear method for the retrieval of sun-induced chlorophyll fluorescence from GOME-2 and SCIAMACHY data. *Atmospheric Measurement Techniques*, 8(6), pp.2589–2608.

Huete, A. et al., 2002. Overview of the radiometric and biophysical performance of the MODIS vegetation indices. *Remote sensing of environment*, 83(1), pp.195–213.

Parazoo, N.C. et al., 2014. Terrestrial gross primary production inferred from satellite fluorescence and vegetation models. *Global change biology*, 20(10), pp.3103–3121.

Parazoo, N.C. et al., 2013. Interpreting seasonal changes in the carbon balance of southern Amazonia using measurements of XCO2 and chlorophyll fluorescence from GOSAT. *Geophysical Research Letters*, 40(11), pp.2829–2833.

Poulter, B. et al., 2014. Contribution of semi-arid ecosystems to interannual variability of the global carbon cycle. *Nature*, 509(7502), pp.600–603.

Cleverly, J. et al., 2016. Productivity and evapotranspiration of two contrasting semiarid ecosystems following the 2011 global carbon land sink anomaly. *Agricultural and Forest Meteorology*, 220, pp.151–159.

Louis, J. et al., 2005. Remote sensing of sunlight-induced chlorophyll fluorescence and reflectance of Scots pine in the boreal forest during spring recovery. *Remote sensing of environment*, 96(1), pp.37–48.

Rotenberg, E. & Yakir, D., 2010. Contribution of semi-arid forests to the climate system. *Science*, 327(5964), pp.451–454.

Joiner, J. et al., 2014. The seasonal cycle of satellite chlorophyll fluorescence observations and its relationship to vegetation phenology and ecosystem atmosphere carbon exchange. *Remote Sensing of Environment*, 152, pp.375–391.

Ahlström, A. et al., 2015. The dominant role of semi-arid ecosystems in the trend and variability of the land CO2 sink. *Science*, 348(6237), pp.895–899.

Beringer, J. et al., 2016. An introduction to the Australian and New Zealand flux tower network–OzFlux. *Biogeosciences*.

Porcar-Castell, A. et al., 2014. Linking chlorophyll a fluorescence to photosynthesis for remote sensing applications: mechanisms and challenges. *Journal of experimental botany*, p.eru191.

Cherwin, K. & Knapp, A., 2012. Unexpected patterns of sensitivity to drought in three semi-arid grasslands. *Oecologia*, 169(3), pp.845–852.

Dawelbait, M. & Morari, F., 2012. Monitoring desertification in a Savannah region in Sudan using Landsat images and spectral mixture analysis. *Journal of Arid Environments*, 80, pp.45–55.

Flexas, J. et al., 2002. Effects of drought on photosynthesis in grapevines under field conditions: an evaluation of stomatal and mesophyll limitations. *Functional Plant Biology*, 29(4), pp.461–471.

Gilabert, M.A., Garcıa-Haro, F.J. & Melia, J., 2000. A mixture modeling approach to estimate vegetation parameters for heterogeneous canopies in remote sensing. *Remote Sensing of Environment*, 72(3), pp.328–345.

Guanter, L. et al., 2012. Retrieval and global assessment of terrestrial chlorophyll fluorescence from GOSAT space measurements. *Remote Sensing of Environment*, 121, pp.236–251.

Guanter, L. et al., 2014. Global and time-resolved monitoring of crop photosynthesis with chlorophyll fluorescence. *Proceedings of the National Academy of Sciences*, 111(14), pp.E1327–E1333.

Guanter, L. et al., 2015. Potential of the TROPOspheric Monitoring Instrument (TROPOMI) onboard the Sentinel-5 Precursor for the monitoring of terrestrial chlorophyll fluorescence. *Atmospheric Measurement Techniques*, 8(3), pp.1337–1352.

Huang, J. et al., 2015. Accelerated dryland expansion under climate change. *Nature Climate Change*.

Papageorgiou, G.C., 2014. The non-photochemical quenching of the electronically excited state of chlorophyll a in plants: definitions, timelines, viewpoints, open questions. In *Non-Photochemical Quenching and Energy Dissipation in Plants, Algae and Cyanobacteria*. Springer, pp. 1–44.

Joiner, J. et al., 2011. First observations of global and seasonal terrestrial chlorophyll fluorescence from space. *Biogeosciences*, 8(3), pp.637–651.

Ma, X. et al., 2015. Abrupt shifts in phenology and vegetation productivity under climate extremes. *Journal of Geophysical Research: Biogeosciences*, 120(10), pp.2036–2052.

Moran, M.S. et al., 2014. Functional response of US grasslands to the early 21st-century drought. *Ecology*, 95(8), pp.2121–2133.

Ponce-Campos, G.E. et al., 2013. Ecosystem resilience despite large-scale altered hydroclimatic conditions. *Nature*, 494(7437), pp.349–352.

Jones, D.A., Wang, W. & Fawcett, R., 2009. High-quality spatial climate data-sets for Australia. *Australian Meteorological and Oceanographic Journal*, 58(4), p.233.

Scott, R.L. et al., 2015. The carbon balance pivot point of southwestern US semiarid ecosystems: Insights from the 21st century drought. *Journal of Geophysical Research: Biogeosciences*, 120(12), pp.2612–2624.

Yang, X. et al., 2015. Solar-induced chlorophyll fluorescence that correlates with canopy photosynthesis on diurnal and seasonal scales in a temperate deciduous forest. *Geophysical Research Letters*, 42(8), pp.2977–2987.

Yi, C., Wei, S. & Hendrey, G., 2014. Warming climate extends dryness-controlled areas of terrestrial carbon sequestration. *Scientific reports*, 4.

Walther, S. et al., 2015. Satellite chlorophyll fluorescence measurements reveal large-scale decoupling of photosynthesis and greenness dynamics in boreal evergreen forests. *Global change biology*.

Mao, J. et al., 2015. Disentangling climatic and anthropogenic controls on global terrestrial evapotranspiration trends. *Environmental Research Letters*, 10(9), p.94008.